Nano-Newton electrostatic force actuators for femto-Newton-sensitive measurements: System performance test in the LISA Pathfinder mission

M. Armano,[1] H. Audley,[2] J. Baird,[3] M. Bassan,[4] P. Binetruy,[5,§] M. Born,[2] D. Bortoluzzi,[6] E. Castelli,[7,8] A. Cavalleri,[9] A. Cesarini,[10] V. Chiavegato,[8,*] A. M. Cruise,[11] D. Dal Bosco,[8] K. Danzmann,[2] M. De Deus Silva,[1] R. De Rosa,[12] L. Di Fiore,[13] I. Diepholz,[2] G. Dixon,[11] R. Dolesi,[8] L. Ferraioli,[14,†] V. Ferroni,[8] E. D. Fitzsimons,[15] M. Freschi,[1] L. Gesa,[16,§] D. Giardini,[14] F. Gibert,[17,8] R. Giusteri,[2] A. Grado,[18] C. Grimani,[10] J. Grzymisch,[19] I. Harrison,[20] M. S. Hartig,[2] G. Heinzel,[2] M. Hewitson,[2] D. Hollington,[21] D. Hoyland,[11] M. Hueller,[8] H. Inchauspé,[22,3] O. Jennrich,[19] P. Jetzer,[23] B. Johlander,[1] N. Karnesis,[24] B. Kaune,[2] N. Korsakova,[3] C. J. Killow,[25,26] L. Liu,[8] J. A. Lobo,[16,§] J. P. López-Zaragoza,[16] R. Maarschalkerweerd,[20] D. Mance,[14] V. Martín,[16] L. Martin-Polo,[1] F. Martin-Porqueras,[1] J. Martino,[3] P. W. McNamara,[19] J. Mendes,[20] L. Mendes,[1] N. Meshksar,[14] J. Moerschell,[27] M. Nofrarias,[16] S. Paczkowski,[2] M. Perreur-Lloyd,[25] A. Petiteau,[5,3] E. Plagnol,[3] C. Praplan,[27] J. Ramos-Castro,[28] J. Reiche,[2] F. Rivas,[29,8] D. I. Robertson,[25] G. Russano,[30,8] L. Sala,[8] P. Sarra,[31] S. L. Schule-Walewski,[32] J. Slutsky,[7] C. F. Sopuerta,[16] R. Stanga,[33] T. Sumner,[21] J. ten Pierick,[14] D. Texier,[1] J. I. Thorpe,[7] D. Vetrugno,[8] S. Vitale,[8] G. Wanner,[2] H. Ward,[25] P. J. Wass,[21,34] W. J. Weber,[8,‡] L. Wissel,[2] A. Wittchen,[2] C. Zanoni,[8] and P. Zweifel[14]

(LISA Pathfinder Collaboration)

[1]*European Space Astronomy Centre, European Space Agency, Villanueva de la Cañada, 28692 Madrid, Spain*
[2]*Albert-Einstein-Institut, Max-Planck-Institut für Gravitationsphysik und Leibniz Universität Hannover, Callinstraße 38, 30167 Hannover, Germany*
[3]*Université Paris Cité, CNRS, Astroparticule et Cosmologie, F-75013 Paris, France*
[4]*Dipartimento di Fisica, Università di Roma "Tor Vergata" / INFN-Sezione Roma Tor Vergata, I-00133 Roma, Italy*
[5]*IRFU, CEA, Université Paris-Saclay, F-91191 Gif-sur-Yvette, France*
[6]*Department of Industrial Engineering, Università di Trento and Trento Institute for Fundamental Physics and Application / INFN, I-38123 Povo, Trento, Italy*
[7]*Gravitational Astrophysics Lab, NASA Goddard Space Flight Center, 8800 Greenbelt Road, Greenbelt, Maryland 20771, USA*
[8]*Dipartimento di Fisica, Università di Trento and Trento Institute for Fundamental Physics and Application / INFN, I-38123 Povo, Trento, Italy*
[9]*Istituto di Fotonica e Nanotecnologie, CNR-Fondazione Bruno Kessler, I-38123 Povo, Trento, Italy*
[10]*DISPEA, Università di Urbino Carlo Bo, Via S. Chiara, 27 61029 Urbino/INFN, Italy*
[11]*The School of Physics and Astronomy, University of Birmingham, B15 2TT Birmingham, United Kingdom*
[12]*Dipartimento di Fisica, Università di Napoli "Federico II" and INFN-Sezione di Napoli, I-80126, Napoli, Italyy*
[13]*INFN-Sezione di Napoli, I-80126 Napoli, Italy*
[14]*Institut für Geophysik, ETH Zürich, Sonneggstrasse 5, CH-8092 Zürich, Switzerland*
[15]*The UK Astronomy Technology Centre, Royal Observatory, Edinburgh, Blackford Hill, Edinburgh EH9 3HJ, United Kingdom*
[16]*Institut de Ciències de l'Espai (CSIC-IEEC), Campus UAB, Carrer de Can Magrans s/n, 08193 Cerdanyola del Vallès, Spain*
[17]*isardSAT SL, Marie Curie 8-14, 08042 Barcelona, Catalonia, Spain*
[18]*INAF Osservatorio Astronomico di Capodimonte, I-80131 Napoli, Italy and INFN-Sezione di Napoli, I-80126 Napoli, Italy*
[19]*European Space Technology Centre, European Space Agency, Keplerlaan 1, 2200 AG Noordwijk, The Netherlands*
[20]*European Space Operations Centre, European Space Agency, 64293 Darmstadt, Germany*
[21]*Physics Department, Blackett Laboratory, High Energy Physics Group, Imperial College London, Prince Consort Road, London SW7 2BW, United Kingdom*
[22]*Institut für Theoretische Physik, Universität Heidelberg, Philosophenweg 16, 69120 Heidelberg, Germany*
[23]*Physik Institut, Universität Zürich, Winterthurerstrasse 190, CH-8057 Zürich, Switzerland*
[24]*Department of Physics, Aristotle University of Thessaloniki, Thessaloniki 54124, Greece*

[25]*SUPA, Institute for Gravitational Research, School of Physics and Astronomy, University of Glasgow, Glasgow G12 8QQ, United Kingdom*
[26]*Qioptiq, Denbighshire LL17 0LL, United Kingdom*
[27]*Haute Ecole Vallaisanne, CH-1950 Sion, Switzerland*
[28]*Department d'Enginyeria Electrònica, Universitat Politècnica de Catalunya, 08034 Barcelona, Spain*
[29]*Universidad Loyola Andalucóa, Department of Quantitative Methods, Avenida de las Universidades s/n, 41704, Dos Hermanas, Sevilla, Spain*
[30]*INAF Osservatorio Astronomico di Capodimonte, I-80131 Napoli, Italy*
[31]*OHB Italia S.p.A, Via Gallarate, 150–20151 Milano, Italy*
[32]*Thales Alenia Space in Switzerland, CH-8052 Zürich, Switzerland*
[33]*Dipartimento di Fisica ed Astronomia, Università degli Studi di Firenze and INFN-Sezione di Firenze, I-50019 Firenze, Italy*
[34]*Department of Mechanical and Aerospace Engineering, MAE-A, University of Florida, P.O. Box 116250, Gainesville, Florida 32611, USA*

(Received 30 December 2023; accepted 26 March 2024; published 22 May 2024)

Electrostatic force actuation is a key component of the system of geodesic reference test masses (TM) for the LISA orbiting gravitational wave observatory and in particular for performance at low frequencies, below 1 mHz, where the observatory sensitivity is limited by stray force noise. The system needs to apply forces of order 10^{-9} N while limiting fluctuations in the measurement band to levels approaching 10^{-15} N/Hz$^{1/2}$. We present here the LISA actuation system design, based on audio-frequency voltage carrier signals, and results of its in-flight performance test with the LISA Pathfinder test mission. In LISA, TM force actuation is used to align the otherwise free-falling TM to the spacecraft-mounted optical metrology system, without any forcing along the critical gravitational wave-sensitive interferometry axes. In LISA Pathfinder, on the other hand, the actuation was used also to stabilize the TM along the critical x axis joining the two TM, with the commanded actuation force entering directly into the mission's main differential acceleration science observable. The mission allowed demonstration of the full compatibility of the electrostatic actuation system with the LISA observatory requirements, including dedicated measurement campaigns to amplify, isolate, and quantify the two main force noise contributions from the actuation system, from actuator gain noise and from low frequency "in band" voltage fluctuations. These campaigns have shown actuation force noise to be a relevant, but not dominant, noise source in LISA Pathfinder and have allowed performance projections for the conditions expected in the LISA mission.

DOI: 10.1103/PhysRevD.109.102009

I. INTRODUCTION

The ESA mission LISA Pathfinder [1] (LPF), which launched on December 3, 2015 and completed science operations in July 2017, measured the differential acceleration between two free-falling test masses. The experiment was sensitive to stray forces acting on a test mass (TM), which introduce noise into their otherwise geodesic orbits and ultimately limit the sensitivity of a future space observatory for gravitational waves in the 20 μHz–1 Hz band, such as the proposed LISA mission [2].

The main LPF experimental observable, $\Delta g \equiv \frac{f_2}{m_2} - \frac{f_1}{m_1}$, is a gravity gradiometer signal, the differential force per unit mass on two TM separated by $L = 37.6$ cm. The spacecraft (SC) was "drag-free" controlled, with precision cold-gas thrusters, to follow one TM (TM1) along the sensitive x measurement axis (see Fig. 1). The second TM (TM2) was forced to follow TM1; any nonzero Δg had to be compensated with applied forces to avoid accelerating TM2, over time, into the surrounding SC apparatus. The required actuation force (per unit mass) on TM2, g_{2c}, had to be accurately calibrated as part of the signal used to

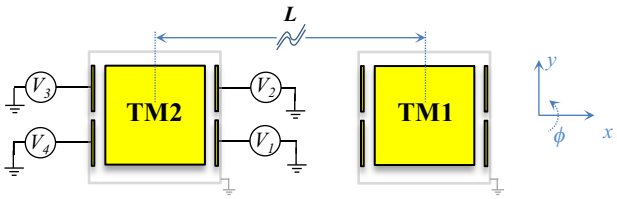

FIG. 1. Cartoon of LPF, with two TM along the sensitive x axis, inside their respective GRS electrode housings. The numbering scheme for the sensor X-face electrodes, used for actuation and sensing of the x and ϕ (rotation around z) degrees of freedom, is shown in the actuation generators for TM2.

*Corresponding author: vittorio.chiavegato@unitn.it
†Corresponding author: luigi.ferraioli@erdw.ethz.ch
‡Corresponding author: williamjoseph.weber@unitn.it
§Deceased.

construct Δg, and any additional force noise introduced by the actuator voltages contributed noise in Δg. Critical sources of low-frequency force noise [3] include additive voltage noise mixing with TM charge and stray electrostatic fields, and multiplicative "gain noise" in the actuator voltage amplitudes, scaling with the applied force levels.

LISA Pathfinder was designed for a differential acceleration "dynamic range" of roughly 1 $\mathrm{nm/s^2}$, while aiming to resolve fluctuations at the 30 $\mathrm{fm/s^2/Hz^{1/2}}$ level at mHz frequencies. At the L1 Lagrange point, far from the $\mu\mathrm{m/s^2}$ differential gravity for a similarly sized gradiometer in low earth orbit, mechanical tolerances in the mass balancing of the local spacecraft "self-gravity" [4] set this $\mathrm{nm/s^2}$ design range. Translated into forces on a 2 kg LPF TM, the actuators must give force authority of order several nN while allowing resolution of femtoNewton (fN) level force variations on time scales of 1000 s.

Actuation forces were required in LPF to balance the DC and slowly varying differential acceleration between the two TM for the three translational axes, plus three angular accelerations for each TM. Forces and torques were commanded as part of the full dynamical "drag-free and attitude-control system" (DFACS), which managed an interconnected mixture of spacecraft thrusting and TM electrostatic actuation [5–7]. The electrostatic actuation system also had to coexist with a TM position readout at the 2 $\mathrm{nm/Hz^{1/2}}$ level [8]. Sensing and actuation capabilities were needed on all six degrees of freedom (d.o.f.), though a higher precision interferometer [9,10] substituted capacitive sensing on the critical science measurement axis. For LPF and LISA, as in geodesy missions like GOCE [11] and tests of gravity like GPB [12] and MICROSCOPE [13], sensing and force actuation are combined into a single electrostatic sensor with the conducting TM surrounded by a conducting housing with an array of electrodes. The design of the LPF "gravitational reference system" or GRS [14,15]—the TM, electrode housing and associated sensing/actuation electronics—differs from the electrostatic accelerometers used in the missions cited in several ways, all motivated by the extremely low-force noise requirements for LISA and LPF. Specifically, it employs a larger and heavier test mass, uses a larger TM-electrode separation—a 4 mm gap on the most sensitive x axis—and eliminates the discharge wire employed in all of the previously cited missions except GPB, in favor of a UV photoelectric discharge system [16].

The required 2 $\mathrm{nm/Hz^{1/2}}$ capacitive sensing has been demonstrated with the LPF TM held in place before release into free-fall [8], while the role of the GRS as a sensor and actuator has been validated in the overall LPF DFACS control [5–7,17]. This article addresses the details of the electrostatic force actuation system for LISA, as designed and tested in the LISA Pathfinder mission.

The article first presents, in Sec. II, the actuation system design, from its specific features to limit electrostatic force noise and its conceptual design, to the high-level circuit implementation. This section includes an overview of the in-flight use conditions encountered in LISA Pathfinder and some key elements of its calibration and verification as part of the LPF differential acceleration measurement chain.

The following two sections form the experimental core of this paper and present the models and measurement campaigns used to quantify two critical force noise sources arising in the electrostatic actuation system: actuation gain fluctuations (Sec. III) and low-frequency additive voltage noise (Sec. IV). Tests were performed in the true in-orbit LPF conditions, which included a background Δg that was always within 25 $\mathrm{pm/s^2}$ of zero, more than an order of magnitude below the $\mathrm{nm/s^2}$ level discussed above, due to successful spacecraft gravitational balancing. This allowed lowering the actuation force "authority," which, as will be discussed in this paper, was of fundamental importance in pushing the ultimate differential acceleration noise down to the 2 $\mathrm{fm/s^2/Hz^{1/2}}$ level at mHz frequencies [18]. Quantifying the actuator noise required application of larger, balancing forces to increase the effect of actuation voltage fluctuations. Likewise, "in-band" additive voltage noise was quantified by measuring acceleration noise with an intentionally charged TM.

We note that the conversion of actuation voltage fluctuations into force noise, described in Secs. III and IV, is relatively straightforward. Additionally, the actuation electronics was subject to pre-flight electronic noise tests on ground. However, a full test measuring force and torque noise from the actuation system, in the complete flight conditions with two TM in multiaxis free-fall, allows a direct validation including correlations and other possible effects escaping the model. Additionally, as for other precision experiments in space, a large time—roughly 6 years for the LPF electronics—and a launch separates the ground tests from flight performance, making *in situ* measurements, such as those presented here, a key part of a reliable experimental noise model.

In Sec. V we use the results of these measurement campaigns to make a projection of the contribution of actuation noise to the LPF differential acceleration measurement Δg and to the acceleration noise of a single TM in experimental scenario of the LISA mission. In contrast with LPF, LISA does not require force actuation along the interferometer x "science axis" used for measuring the gravitational-wave induced tidal acceleration. It does however need angular torque control applied with electrostatic fields along the critical x axis, and these are a potentially important source of TM acceleration noise that can impact the mission science return.

The article ends with some final comments on the role of actuator noise in the overall acceleration noise performance for LPF and LISA, as well as a consideration on the uniqueness of LISA Pathfinder as a test bench for the measurement of small forces and torques.

II. GRS ELECTROSTATIC ACTUATION SYSTEM DESIGN AND ROLE IN LPF Δg MEASUREMENT

The LPF observable Δg is constructed from Newtonian dynamics and telemetry for the commanded forces and interferometric readouts for the relative TM displacement, $\Delta x \equiv x_2 - x_1$, and the relative TM1-SC displacement, x_1 [1]:

$$\Delta g = \Delta\ddot{x} - \lambda g_{2c} + \Delta\omega^2 x_1 + \omega_2^2 \Delta x. \tag{1}$$

The leading terms are the measured acceleration $\Delta\ddot{x}$ and commanded force g_{2c}, scaled by calibration factor λ, which dominates at frequencies below the roughly 1 mHz unity-gain controller bandwidth. Smaller corrections due to coupling of the two TM to the SC motion are approximated as elastic with effective spring constants $m_1\omega_1^2$ and $m_2\omega_2^2$ and differential "stiffness" $\Delta\omega^2 \equiv \omega_2^2 - \omega_1^2$. For simplicity, we have omitted from Eq. (1) the inertial force terms that are corrected in the standard LPF analysis [1,18], most importantly for the centrifugal force along x from the noisy rotation of the LPF spacecraft, which is calculated using the angular control data. Ultimately the TM2 electrostatic actuation force per unit mass g_{2c} is used to compensate all low-frequency differential accelerations along x, from real forces and any accelerated-spacecraft reference frame effects.

The accuracy, linearity, and stability of the actuator gain—factor λ in the subtraction of the applied force—set the accuracy with which Δg is measured, most significantly at low frequencies below 1 mHz. The applied electrostatic forces also depend on the TM position, with the resulting force gradients contributing to the stiffness ω_1^2 and ω_2^2; these must be reliably known and stable for accurate calculation of Δg. Finally, and most importantly, unmodelled force noise associated with the actuation fields—due to actuation gain fluctuations or to additive circuit voltage noise that mixes with stray electrostatic fields—contributes directly to the noise in Δg along with any other external force noise on the TM.

A. Actuation conceptual design

The actuation design employs audio frequency voltages, in the 60–270 Hz band, to create the needed DC and slowly varying electrostatic forces needed for dynamical control of the TM-spacecraft system. This exploits the quadratic force-voltage dependence, $F \propto \Delta V^2$, to give a DC force that depends only on the carrier amplitude plus a force at twice the carrier frequency, decades above the mHz LPF measurement band (the electrostatic force model and actuation algorithm are presented in Appendix A). This is chosen to limit the force errors and low frequency force noise from stray fields from TM charge and surface "patch" potentials [19–22]: any steady or slowly varying stray potential difference mixes with the applied audio carrier to produce a force, and force noise, safely outside the LISA band around the carrier frequency. Considering stray potentials of order 100 mV, and their noise, use of AC carriers is a necessary design innovation for LPF.

Referring to the X electrode configuration in Fig. 1, the LPF actuation scheme follows,

$$\begin{aligned} V_{1c}(t) &= V_{1x}\sin\omega_x t + V_{1\phi}\sin\omega_\phi t, \\ V_{2c}(t) &= -V_{1x}\sin\omega_x t + V_{2\phi}\cos\omega_\phi t, \\ V_{3c}(t) &= V_{2x}\cos\omega_x t - V_{1\phi}\sin\omega_\phi t, \\ V_{4c}(t) &= -V_{2x}\cos\omega_x t - V_{2\phi}\cos\omega_\phi t, \end{aligned} \tag{2}$$

with similar expressions for the Y electrodes (degrees of freedom y and θ) and Z electrodes (d.o.f. z and η). The subscript "c" is employed here in $V_{jc}(t)$ to indicate the *commanded* voltage on electrode j.

The applied x actuation voltages V_{1x} and V_{2x} yield a total time-average force proportional to $(V_{1x}^2 - V_{2x}^2)$ and a force gradient proportional to $(V_{1x}^2 + V_{2x}^2)$. The LPF "constant stiffness" actuation algorithm fixes $V_{1x}^2 + V_{2x}^2 \equiv V_{\mathrm{MAX}_x}^2$, allowing application of force per unit mass g_c in the range $\pm g_0 = \pm\frac{1}{2m}\frac{\partial C_X^\star}{\partial x} V_{\mathrm{MAX}_x}^2$, with

$$V_{1x/2x} = \left[\frac{M(g_0 \pm g_c)}{\left|\frac{\partial C_X^\star}{\partial x}\right|}\right]^{1/2}, \tag{3}$$

where $\frac{\partial C_X^\star}{\partial x}$ is the relevant capacitance derivative for an X electrode (see Appendix A) and M the mass of the nominally identical test masses. The desired force is thus produced by unbalancing the electrostatic forces pulling on opposing sides of the TM. The resulting x axis stiffness contribution is independent of the applied force g_c,

$$\omega_{xx}^2 = -g_0\frac{\left|\frac{\partial^2 C^\star}{\partial x^2}\right|}{\left|\frac{\partial C^\star}{\partial x}\right|} \approx -\frac{2g_0}{d_x}, \tag{4}$$

where d_x is the gap between the X electrodes and the TM, assumed equal on opposing sides.

Expressions analogous to Eqs. (3) and (A14) are obtained for the voltages $V_{1\phi/2\phi}$ and stiffness associated with electrostatic actuation for the ϕ rotational degree of freedom, described by the commanded torque (per unit moment of inertia) γ_{ϕ_c} within the torque authority range of $\pm\gamma_{\phi_0}$, both with units of angular acceleration, $/\mathrm{s}^2$. Both x and ϕ actuation contribute individually to the stiffness along both the x and ϕ d.o.f. The constant stiffness algorithm allows a fixed and calculable (negative) elastic coupling in the control dynamics and eliminates a first-order cross- coupling between ϕ torques and x acceleration for an off-center TM.

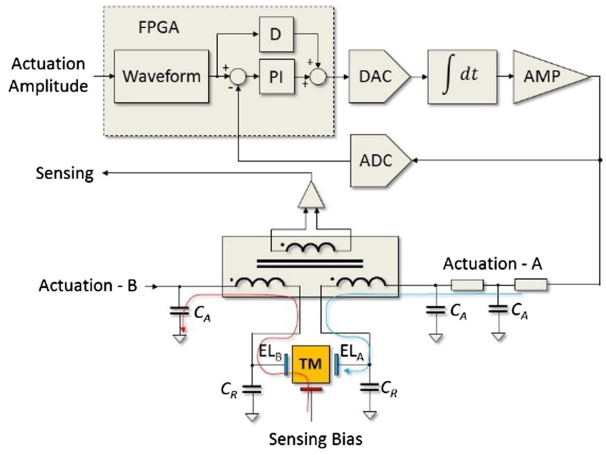

FIG. 2. Circuit block diagram featuring sensing and actuation elements for two opposing electrodes (a single sensing channel). Red and blue curves indicate current paths for, respectively 100 kHz sensing and audio/DC actuation.

Voltage waveforms are applied with opposite phase [$\pm V_{1x}$ on electrodes 1 and 2, for instance, see Eq. (2)], to eliminate any induced TM potential, at least for a centered TM. Orthogonal waveforms (cos/sin) and different frequencies ($\frac{\omega_x}{2\pi} = 60$ Hz and $\frac{\omega_\phi}{2\pi} = 270$ Hz) avoid cross-talk between the different actuation degrees of freedom.

B. Actuation circuit implementation

The actuation circuit implementation is sketched as part of the sensing/actuation "front-end electronics" in Fig. 2. Sensing and actuation operate simultaneously with the same electrodes, with currents sharing the primary windings of the sensing differential transformer [14]. Capacitive sensing uses a "contact free" injection of a 100 kHz bias on the TM, with the difference of current flowing through opposing pairs of electrodes measured by a resonant differential transformer bridge followed by transimpedance amplifier and homodyne detection scheme to give six gap-sensing displacement readouts.

Audio frequency actuation voltages are applied to the electrodes through the primary windings, with two passive RC stages (with C_A) used to limit interference with the 100 kHz position readout. Digital "target" actuation voltages are generated in a field programmable gate array (FPGA), where audio waveforms are synthesized from commanded peak amplitudes and then summed with the DC voltages, with DC and audio amplitudes updated at the 10 Hz experimental sampling rate, sufficient for the force controller loops. The actuation outputs are stabilized by a $\Sigma - \Delta$ loop using a DAC, integrator, 96 kHz ADC, and digital PID controller, effectively tying the actuation waveform generator stability to that of the ADC voltage reference, which is the same for groups of four actuation channel circuits located on a single board, such as for the four electrodes used for sensing and actuating x and ϕ electrodes, as illustrated in Fig. 1.

Based on the DC force balancing requirements [4], the LPF actuation system was designed for an x actuation authority of $g_0 = 1.15$ nm/s^2 (2.2 nN) for TM2—with no TM1 x actuation—and ϕ authority $\gamma_{\phi_0} \approx 15$ nrad/s^2 (10.4 pNm) for both TM. These are given also in Table I as the "nominal" configuration, used at the start of the mission and in the second actuation noise trial described in Sec. III. Given the LPF GRS X electrodes, with surface area 530 mm^2 and gap $d_x = 4$ mm, this corresponds [Eqs. (3) and (A14)] to $V_{\mathrm{MAX}_x} \approx 4.5$ V and $V_{\mathrm{MAX}_\phi} \approx 2.9$ V (peak amplitudes), with associated x-axis electrostatic stiffness contributions of approximately -660×10^{-9}/s^2 and -270×10^{-9}/s^2. The maximum possible total instantaneous voltage, 7.4 V, fits comfortably into a roughly 10 V envelope allowed by the actuation electronic science mode AC voltage range. The actuation circuitry also allowed for several volt DC voltages applied to any sensing / actuation electrode, for compensating stray DC voltages, measuring TM charge, and biasing the UV discharge [16,23].

The actuation nominal bit resolution was 153 μV, yielding an effective force quantization of order 100 fm/s^2 with this nominal force authority (1.15 nm/s^2). To smooth the resulting "force bit" steps in the commanded force, a software $\Sigma - \Delta$ loop in the TM2 dynamic control loop was implemented in the on-board computer, which dithers the commanded voltage between adjacent voltage levels, reducing the effective bit size by a factor 30 on 100 s time scales.

TABLE I. Summary of actuation gain noise experiments for four different configurations, including measurement duration and average commanded force and force authorities—for instance g_{1c} and g_{10}—and analogously for torque (e.g. $\gamma_{\phi_{1c}}$ and $\gamma_{\phi_{10}}$) [24].

			g_{1c}	g_{10}	$\gamma_{\phi_{1c}}$	$\gamma_{\phi_{10}}$	g_{2c}	g_{20}	$\gamma_{\phi_{2c}}$	$\gamma_{\phi_{20}}$
Experiment	Name	Time hours	pm/s^2		prad/s^2		pm/s^2		prad/s^2	
1	UURLA	61	0	0	−980	2170	−3	26	130	1450
2	Nominal	46	0	0	−960	15040	−3	1140	150	15040
3	Big	46	0	2590	−860	15040	−3	2590	90	15040
4	Big off	46	2060	2590	−820	15040	2060	2590	140	15040

C. Actuation use, functionality, and performance in LISA Pathfinder

Due to the superior gravitational balancing actually achieved in the as-flown LPF, the actual needed force and torque actuation levels were considerably below the "nominal" levels, most notably between -25 pm/s^2 to $+12$ pm/s^2 in the TM2 x force (except during the actuation noise campaign described in the next section). This allowed lowering the force authority in x to $g_0 \approx 26$ pm/s^2 ($V_{\mathrm{MAX}_x} \approx 0.7$ V). The ϕ controller authorities were also lowered as allowed by the smaller levels of torque needed, with the typical TM1 and TM2 authorities of roughly 2.2 nrad/s^2 and 1.5 nrad/s^2 ($V_{\mathrm{MAX}_\phi} \approx 0.9$ and 0.7 V). The resulting total electrostatic x-axis stiffness from actuation was roughly -40×10^{-9}/s^2 for both TM. This configuration, known as UURLA and described on line 1 of Table I, was used for the main noise measurements in LPF [1,18].

Periodically, and upon change in the actuation authorities, the x_2 actuation calibration factor (λ) and the stiffness coefficients (ω_2^2 and $\Delta\omega^2$) were calibrated with a "system identification" experiment in which the control set points for the x positions of the two TM were commanded to oscillate sinusoidally over a range of frequencies from 1 mHz to 50 mHz and with typical amplitudes up to 10 nm [17]. Parameters λ, ω_2^2, and $\Delta\omega^2$ are then extracted by fitting the time series of g_{2c}, x_1, and Δx to the model in Eq. (1). The gain factor λ has been found to be stable over the year of data analyzed, at a level approaching 0.01% and with a mean value within 1% of that calculated from the voltage source design and the electrostatic force model. The measured dependence of the stiffness on force and torque authorities g_0 and $\gamma_{\phi 0}$, independent of the applied forces and torques, verifies the "constant stiffness" algorithm and corresponds with the electrostatic model to within roughly 5% [17,25]. The LPF in-flight dynamical calibration of Δg, including the actuator calibration and stiffness, has been addressed in detail in a dedicated paper [17].

An additional "calibration tone" experiment has been performed (Fig. 3) in which a sinusoidally oscillating force at 7 mHz was superimposed on the controller force command in g_{2c}, with amplitude of 20 fN and then 100 fN. The presence of the "out-of-loop" force should not be visible in an accurately calculated time series of Δg, including accurate and stable calibration factor λ [see Eq. (1)]; the commanded oscillation in the force g_{2c} produces a corresponding oscillating differential acceleration $\Delta\ddot{x}$ that cancels in Δg, which thus includes only the external, "out of loop" residual forces on the TM. This is in fact observed, with the resulting trace of Δg found to be compatible with the background statistical noise and residuals at the modulation frequency below the fm/s^2 level—and less than 1%—in every cycle, demonstrating the fm/s^2 accuracy of the differential accelerometer with

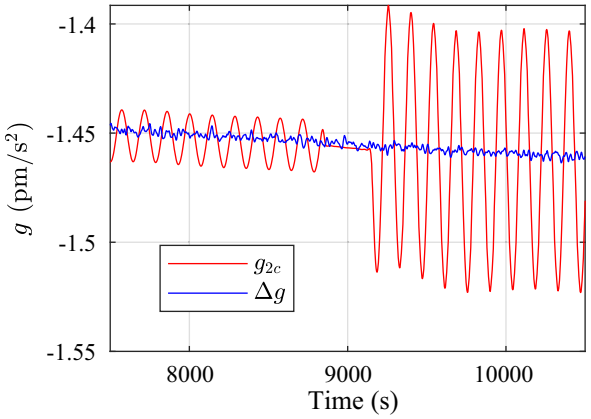

FIG. 3. Time series of applied force g_{2c} and resulting differential acceleration Δg during the "calibration tone" experiment described in the text.

actuation. We note that obtaining this accurate calibration and linearity was not automatic and required a correction to a subtle but deterministic roundoff error in the actuation DAC circuitry. This correction is not addressed here but was critical in reaching the best performances obtained in LPF [18] and is addressed in detail in a dedicated paper [26].

A final aspect of the actuation performance is force crosstalk between the various electrostatically-actuated degrees of freedom. The constant stiffness and symmetric waveform design presented here aims to minimize "leakage" of applied forces into other degrees of freedom, but residual actuation crosstalk [27,28] remains, due to geometric imperfections and, most importantly for the critical ϕ torque to x force, differences in the voltage gains between the four X electrodes. A measured residual coupling of spacecraft rotational acceleration—estimated by the applied electrostatic torques, $\gamma_{\phi_{\mathrm{SC}}} \approx \gamma_{\phi_c}$—with a cross-coupling coefficient of typically $\beta_{\phi x} \equiv \frac{\Delta g}{\gamma_{\phi_c}} \approx 150$ μm [17,18]. This could be attributed to a gain imbalance, of order 0.5%, between the different electrode actuation circuits, though such an effect would be essentially indistinguishable from other Euler-force effects in the LPF data. This gives a rough level for actuation crosstalk effects, possibly relevant also in LISA.

III. ACTUATION GAIN FLUCTUATIONS: NOISE MODEL, EXPERIMENT DESIGN, AND RESULT

A. Actuation gain noise model

In the LPF noise model, the most critical actuation force noise arises in in-band gain or multiplicative amplitude fluctuations [3]; even in the event of constant commanded force—and thus commanded voltage amplitudes V_{1x} and V_{2x}, Eq. (3)—fluctuations in the true carrier amplitude at the electrode result in a fluctuating force. With $F \propto V^2$, the force fluctuations caused by an actuator

electrode can be described in terms of the relative voltage fluctuation, or gain fluctuation, $\alpha \equiv \frac{\delta V}{V}$,

$$\delta F = 2F\frac{\delta V}{V} = 2F\alpha. \tag{5}$$

If $\alpha(t)$ is the same for all four circuits responsible for the TM2 x force, as expected for fluctuations in their common DC voltage reference, the resulting noise in the Δg measurement depends only on the actuator stability and on the commanded *net* force,

$$S^{1/2}_{\Delta g(\mathrm{ACT})} \approx 2|g_c|S^{1/2}_{\alpha}. \tag{6}$$

This was used to set requirements on the LPF self-gravity differential force, $\Delta g_{DC} \leq 1.3\ \mathrm{nm/s^2}$, and the actuation gain noise, $S^{1/2}_{\alpha} \leq 2\times 10^{-6}/\mathrm{Hz}^{1/2}$ at 1 mHz [14,29].

Uncorrelated amplitude fluctuations between the different electrodes complicate this picture, as understood later in LPF development [3]; Eq. (5) is valid on an *electrode-by-electrode* basis such that the force noise depends not only on the net applied force on TM2 g_{2c} but also on the individual electrode voltage levels, and thus also on the authority g_0 and the applied torque and torque authorities, $\gamma_{\phi c}$ and $\gamma_{\phi 0}$ for both TM. For instance, uncorrelated fluctuations in the amplitudes of the carrier voltages $\pm V_{1\phi}$ applied to electrodes 1 and 3 to create a positive ϕ torque, will give rise to asymmetric x-force fluctuations that do not cancel and which thus contribute to the noise in Δg.

Considering the eight relevant actuator gains and any possible correlations between them, in general there would be 36 relevant cross-spectrum terms at each frequency. Considering an experimental campaign with limited duration and number of experimental configurations, we propose here a minimal model, including only terms with known physical origin to describe, and then fit, the acceleration noise spectrum. This possible, but not unique, parametrization of the multiplicative gain fluctuations for electrode j of TM i with commanded voltage V_{ijc} is

$$V_{ij}(t) = V_{ijc}(t)[1 + \alpha(t) + \alpha_i(t) + \alpha_{ij}(t)] + v_{ij}(t), \tag{7}$$

where we include:

(i) α, a gain fluctuation common to all eight X electrodes for the two TM, such as a systematic dependence on the GRS FEE box temperature (our experiments however will not be sensitive to this term);
(ii) α_i, to become α_1 and α_2, which is a "TM correlated" gain fluctuation, corresponding to fluctuations in the single voltage reference voltage common to the four circuits used for x/ϕ actuation on a single TM;
(iii) α_{ij}, independent gain fluctuations for electrode j of TM i, uncorrelated between the eight electrodes.

The role of additive noise v_{ij} mixing with the carrier voltages is discussed separately, in the next subsection.

In this model the resulting noise in Δg is a sum of contributions from 11 independent noise generators,

$$\Delta g^{\mathrm{ACT}}(t) = a\alpha(t) + \sum_{i=1,2} a_i\alpha_i(t) + \sum_{ij} a_{ij}\alpha_{ij}(t) \tag{8}$$

with coefficients

$$\begin{aligned} a &= 2(g_{2c} - g_{1c}) = 2(\Delta g),\\ a_1 &= -2g_{1c},\\ a_2 &= 2g_{2c},\\ a_{21} &= \frac{1}{2}(\bar{g}_{2c} + g_{20} + R^{\star}_{\phi}\bar{\gamma}_{\phi_{2c}} + R^{\star}_{\phi}\gamma_{\phi_{20}}), \end{aligned} \tag{9}$$

where we take as an example of the independent electrode gain noise terms a_{21} for electrode 1 of TM2, which is used to apply positive x forces and ϕ torques. Here $R^{\star}_{\phi} \equiv \frac{I}{m}\frac{\frac{\partial C^{\star}}{\partial x}}{\frac{\partial C^{\star}}{\partial \phi}} \approx 32$ mm is an effective armlength converting angular into linear acceleration (I is the TM moment of inertia). See Appendix B for a more detailed discussion of this model.

If we consider these 11 noise generators mutually uncorrelated, the resulting noise power spectral density (PSD) is

$$S^{\mathrm{ACT}}_{\Delta g} = AS_{\alpha} + \sum_{i=1,2} A_i S_{\alpha_i} + \sum_{ij} A_{ij} S_{\alpha_{ij}} \tag{10}$$

with coefficients

$$\begin{aligned} A &= a^2 = 4(g_{2c} - g_{1c})^2 = 4(\Delta g)^2 = 4(\Delta g^{\mathrm{DC}})^2,\\ A_1 &= a_1^2 = 4g_{1c}^2 \quad [=0],\\ A_2 &= a_2^2 = 4g_{2c}^2 \quad [=4(\Delta g^{\mathrm{DC}})^2],\\ A_{21} &= a_{21}^2 = \frac{1}{4}(\bar{g}_{2c} + g_{20} + R^{\star}_{\phi}\bar{\gamma}_{\phi_{2c}} + R^{\star}_{\phi}\gamma_{\phi_{20}})^2, \end{aligned} \tag{11}$$

where A_{21} is given as an example of the eight relevant uncorrelated gain noise A_{ij} coefficients. Here the numbers offset in block parentheses at right for the board terms A_1 and A_2 refer to the typical operating conditions of LPF, where the differential DC acceleration Δg^{DC} is balanced by forcing only TM2, with $g_{1c} = 0$ and $g_{2c} \approx -\Delta g^{DC}$.[1]

Board-correlated gain fluctuations, for instance S_{α_2} for TM2 arising from a fluctuating reference voltage, indeed couple to the net applied forces to give force noise, as suggested by Eq. (6). Additionally, however, uncorrelated gain fluctuations for individual electrodes, $S_{\alpha_{ij}}$, introduce noise in Δg related to commanded force and force authority (i.e. $\{g_{2c}, g_{20}\}$) as well as commanded ϕ torques and torque

[1]This "typical" condition is not required, as both TM can have a "common mode" applied force, as in the fourth and final actuation gain noise test (see Table I).

authorities ($\{\gamma_{\phi_{1c}}, \gamma_{\phi_{10}}, \gamma_{\phi_{2c}}, \gamma_{\phi_{20}}\}$). It is thus important to limit also the residual DC torques, gravitational or otherwise, and to reduce the force and torque authorities to the minimum levels that still allow compensation of the DC forces with sufficient margin for the system dynamics.

We stress that, while physically motivated, this parametrization in terms of 11 independent, uncorrelated "noise generators" is not the only possible model; it is a useful construct for quantifying actuation force noise in LPF and LISA, insofar that it is compatible with the data, which will be discussed shortly. Any model with actuator gain noise will however have force noise with a PSD increasing quadratically with the forces and torques applied by the single electrodes [Eq. (5)].

B. Model for mixing of additive actuation noise with actuation carriers

Additive voltage noise near the actuation frequencies mixes with the carrier voltages to "down-convert" into low-frequency force noise. The relevant "cross-terms" in the squared actuation voltage have the form, for electrode 1 of a TM as an example,

$$\delta g(t) = \frac{1}{M}\left|\frac{\partial C_X^{\star}}{\partial x}\right| v_1(t)[V_{1x}\sin\omega_x t + V_{1\phi}\sin\omega_\phi t]. \quad (12)$$

Summing over the four X electrodes for that TM and considering the conversion of commanded force/torque into actuation voltage amplitude, the down-converted in-band TM acceleration noise will be

$$S_g = \frac{2\left|\frac{\partial C_X^{\star}}{\partial x}\right|}{M}[S_{v_n}(\omega_x)g_0 + S_{v_n}(\omega_\phi)R_\phi^{\star}\gamma_{\phi_0}]. \quad (13)$$

In contrast with the mHz gain noise, the broadband noise is rather easy to model with circuit design and component data. In the experiment analysis and noise projections that follow, we calculate and insert this acceleration noise contribution, assuming $S_{v_n}^{1/2}(\omega_x) \approx S_{v_n}^{1/2}(\omega_\phi) \approx 2\,\mu\mathrm{V/Hz^{1/2}}$, based on ground measurements.

The additive audio frequency noise thus gives a white noise, at least in the relevant mHz band, with noise power proportional to the applied force and torque authorities g_0 and γ_{ϕ_0}, while the gain noise terms scale quadratically with the forces, as g_0^2 and $\gamma_{\phi_0}^2$. Gain noise dominates over this additive voltage noise for Δg at mHz and sub-mHz frequencies in typical LPF science (UURLA) conditions, even more so in the actuation noise test, presented next, with larger force levels.

C. Actuation noise measurement campaign

Quantifying the actuation gain fluctuations, at least for the x/ϕ actuators that can give x-force noise, is important for the LPF Δg noise budget and for a parametric projection to LISA. We did this in LPF by observing the increase in the differential acceleration noise in a series of tests with increasing forces and torques. The changes in the applied forces and torques are constrained by the need to maintain the same quasistatic torques, to keep each TM aligned to the spacecraft, and the same *differential* applied forces, to hold the TM separation fixed.

In addition to the differential x acceleration Δg, our analysis of the tests considers also the measured differential angular acceleration, $\Delta\gamma_\phi$, which is sensitive to the same $8X$ electrode actuators and thus to the same gain fluctuations α, α_i, and α_{ij}. This is defined as

$$\Delta\gamma_\phi = \ddot{\phi}_2 - \ddot{\phi}_1 - \gamma_{\phi_{2c}} + \gamma_{\phi_{1c}} + \omega_{\phi_2}^2\phi_2 - \omega_{\phi_1}^2\phi_1. \quad (14)$$

The noise in $\Delta\gamma_\phi$ from actuation gain fluctuations is modeled analogously to that in Δg [Eqs. (10) and (11)],

$$\Delta\gamma_\phi^{\mathrm{ACT}}(t) = b\alpha(t) + \sum_{i=1,2} b_i\alpha_i(t) + \sum_{ij} b_{ij}\alpha_{ij}(t) \quad (15)$$

with coefficients b, b_i and b_{ij} coupling gain noise into angular acceleration. For instance $b = 2\Delta\gamma_\phi^{DC}$ and $b_1 = 2\gamma_{\phi_{1c}}$, while for the independent fluctuations in the gain of, for instance, electrode 1 of TM2, we find $b_{21} = R_\phi^{\star}a_{21}$ (see Appendix B for a complete description of the actuation noise model and analysis techniques).

This allows analysis of the differential acceleration noise $S_{\Delta\gamma_\phi}$ with coefficients B, B_i, and B_{ij} in direct analogy with the translational differential acceleration noise coefficients A of Eq. (11). Additionally, it allows an analysis of the cross-spectrum $S_{\Delta g,\Delta\gamma_\phi}$ representing the correlation between the fluctuations of differential translational and rotational accelerations. For instance a gain fluctuation α_{i1} or α_{i4}, on an electrode 1 or 4 in Fig. 1—the "bottom" electrodes in this view—will produce correlated fluctuations in Δg and $\Delta\gamma_\phi$ with the same sign. Thus $S_{\Delta g,\Delta\gamma_\phi} > 0$, while a gain fluctuation on the "top" electrodes 2 or 3 will produce anticorrelated fluctuations and thus a negative cross-spectrum. Including $S_{\Delta g,\Delta\gamma_\phi}$ in our analysis thus further helps distinguish between the electrodes creating force noise.

Noise measurements were performed in four different actuation configurations over 10 days during May 2016. The net forces/torques and authorities are shown in Table I, and the corresponding electrode-by-electrode force vectors are shown in Fig. 4 along with the A and B sensitivity coefficients. The first experiment (UURLA) employs the typical LPF science configuration used in the published differential acceleration noise data [1,18], with minimum authorities. Configurations 2 and 3 increase the force and torque authorities (g_0 and γ_0), first to the "nominal" level (Exp. 2), and then (Exp. 3) a further increase in the force authority to 2.6 $\mathrm{nm/s^2}$ on each TM ("big" configuration).

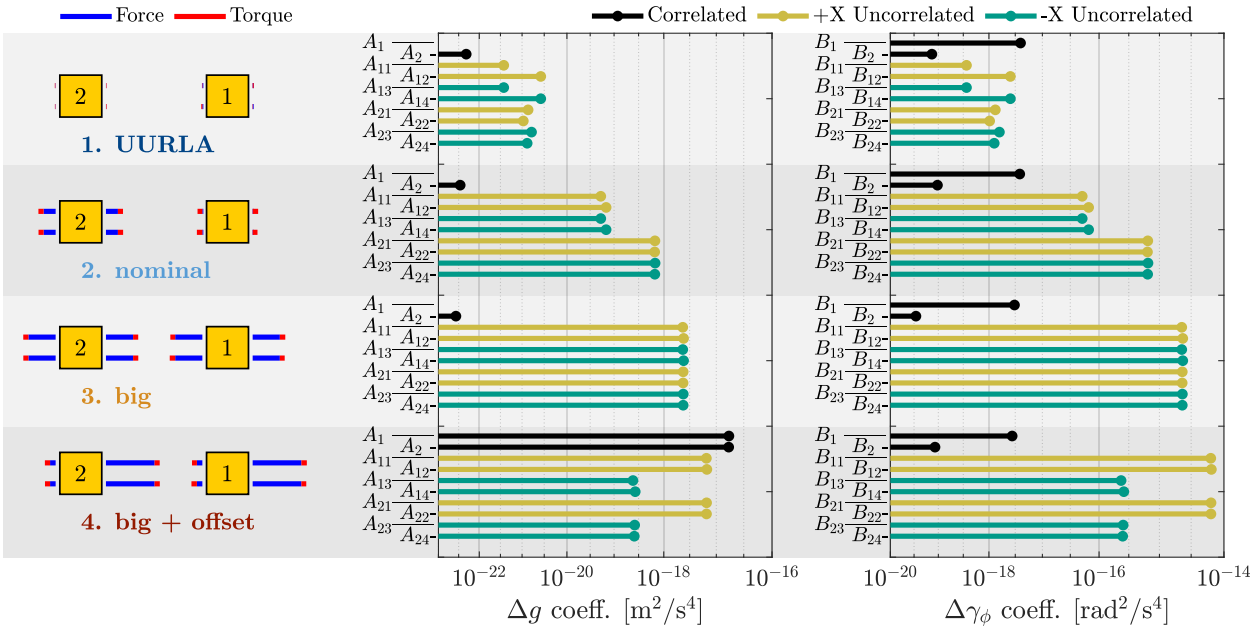

FIG. 4. At left, illustration of the applied force vectors for every electrode in the four tested actuation configurations, including force and torque contributions in, respectively, blue and red. At right are plotted the force and torque sensitivity coefficients for correlated (A_i and B_i, black) and uncorrelated actuation gain noise (A_{ij} and B_{ij}), with $+X$ (electrodes 1 and 2 in Fig. 1) and $-X$ (electrodes 3 and 4) actuators shown in dark yellow and in green. The coefficients are calculated using the averaged commanded forces and torques and force/torque authorities, as described in the text.

These increased authority experiments essentially leave the net applied forces and torques (g_{ic} and $\gamma_{\phi ic}$) unchanged but increase the forces on the single electrodes, increasing sensitivity to uncorrelated gain fluctuations (coefficients A_{ij} and B_{ij}). Experiment 4 adds an applied "out-of-loop" offset force ($\approx$2.1 nm/s^2) to TM1 to produce, in closed loop, a common mode force on both TM (and thus also a net spacecraft acceleration). This final experiment increases sensitivity both to the $+X$ actuators and to the board-correlated fluctuations for each TM (A_i); the degeneracy between these two effects in Δg is broken by observing the differential angular acceleration noise, as the applied net DC torques—and thus the sensitivity to board-correlated fluctuations through B_i—are unchanged. With more experimental time available, further measurements could have employed large negative forces or other configurations to help isolate individual noise contributors.

The dataset can be thought of as a two-channel (x and ϕ) acceleration noise test of three "enhanced-actuation" configurations producing noise above a background level measured in the first UURLA configuration. The experiments performed are sensitive to all of the 11 actuation gain noise generators in the proposed model; some combinations of these noise PSD are clearly resolved, while others are found to be compatible with zero to within upper limits that place significant experimental bounds on the circuitry gain noise.

The measured acceleration noise levels in Δg and $\Delta\gamma_\phi$ are shown in Fig. 5. The solid curves are standard Welch periodograms, with 50% overlapping 110,000 s Blackman-Harris window, while the discrete data points, with error bars, are calculated with a variable window length adapted to the frequency, as in Ref. [18]. For the three "enhanced actuation" experiments, two 110,000 s windows are used for the minimum frequency point at 36.4 μHz, nine 33,000 s windows at 121.2 μHz, and 76 4300 s windows for the point at 0.93 mHz.

The visible progressive increase in the acceleration noise over the four experiments merits comment before discussing a fit to the actuation noise model:

(i) The noise increase with force authority (g_0, γ_0), clearly resolved from Experiment 1 UURLA (dark blue) to the nominal (Experiment 2, light blue) and "big" (Experiment 3, orange) tests, quantifies the key role of uncorrelated gain fluctuations. A gain fluctuation correlated across all four TM1 or TM2 actuators (α_1 or α_2) would not increase force or torque noise in these tests where the net applied forces and torques are essentially left unchanged.

(ii) The measured acceleration noise in the Experiment 2 "nominal" configuration would have set the LPF acceleration noise floor had the gravitational balance not allowed lowering the force authorities. At 0.1 mHz, reducing the authorities to the UURLA configuration improves the overall acceleration

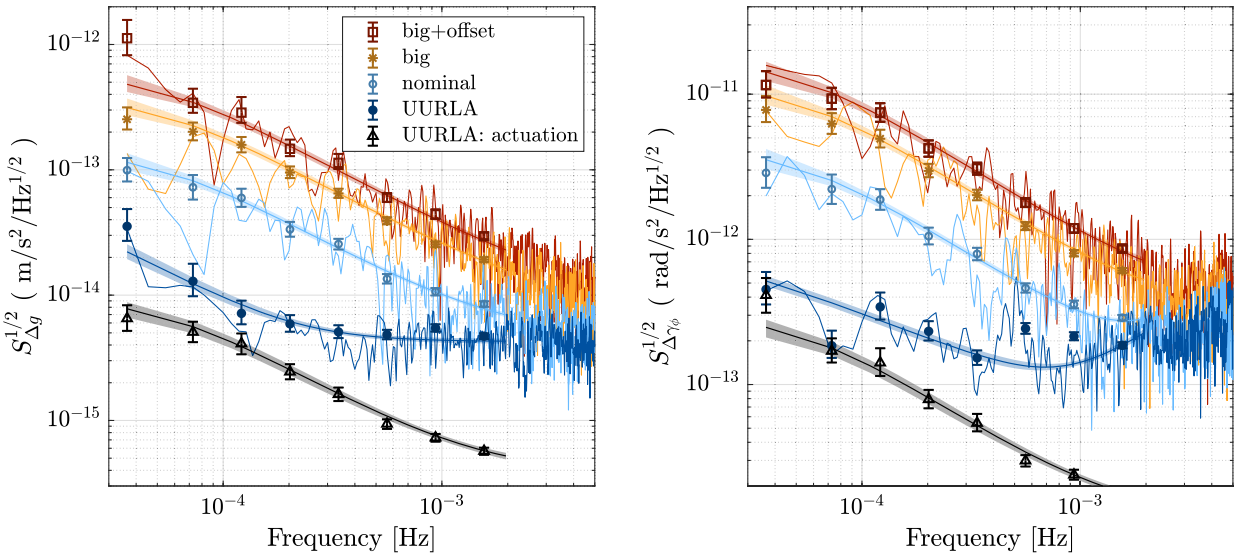

FIG. 5. Experimental data for noise PSD for Δg and $\Delta\gamma_\phi$ in the four different actuation configurations measured, including a fit to the actuation noise model (described in the text and in Appendix B), performed both for a "smooth" model of the noise frequency dependence (colored bands) and on a frequency by frequency analysis (individual points with error bars). Both plots contain (dark gray) the model prediction for the actuation gain noise contribution in the UURLA low-force authority configuration used in the published benchmark plots for LPF acceleration noise [1,18].

noise floor by roughly a factor 50 in noise power, a substantial decrease allowing a much more stringent experimental anchor to the LISA low-frequency mission requirements [2].

(iii) The modest increase in both Δg and $\Delta\gamma_\phi$ upon application of a large offset force, from Experiment 3 (orange) to Experiment 4 (red), confirms the domination of uncorrelated gain fluctuations over the board-correlated gain fluctuations. A large correlated noise contribution (α_1 or α_2) would have produced a more sizable increase in $S_{\Delta g}$ without any effect on $S_{\Delta\gamma_\phi}$.

A fit of the acceleration noise dataset to the actuation noise model described by Eq. (10) [more generally by Eq. (B2) in Appendix B] is also shown in Fig. 5, with the fit analysis first performed separately at each frequency (discrete points) and then to a phenomenological analytical frequency dependence model (smooth bands). The fit, performed using a Bayesian Markov chain Monte Carlo (MCMC) approach, uses all the actuation terms in Eq. (B2), plus background acceleration noise that is independent of the applied actuation forces and torques. This background acceleration noise includes also the first actuation term for completely correlated noise S_α [Eq. (10)], as the coupling to acceleration noise—via Δg^{DC} in translation and $\Delta\gamma_\phi^{DC}$ for rotational—is virtually unchanged across the four experiments.

Not all of the ten actuation noise generators are resolved in this analysis, and a fit to a reduced set of parameters would be sufficient to describe measured noise in the four experiments; nonetheless, we include all these terms in the fit in order to predict the actuation noise in other LPF configurations with arbitrary applied force and torque values. Additionally, while we do not resolve the noise in every individual noise generator, we do put relevant experimental upper limits on *all* noise generators; no single noise generator can create more noise than the total noise observed in the experimental data for Δg and $\Delta\gamma_\phi$, and this constrains the upper limit on the PSD of each single noise generator.

The MCMC fitting technique considers a likelihood with the proper statistics for Welch periodogram estimates of PSD and cross-PSD (CPSD) for Gaussian noise processes [30,31] and is described in detail in Appendix B, along with assumed priors on parameters and typical observed posterior distributions. We note here that the fit is parametrized in terms of averaged levels of board-correlated gain noise (S_{α_C}) and uncorrelated individual electrode gain noise ($S_{\alpha_{UC}}$), with secondary parameters (μ_l) describing the division of noise into the specific TM or specific electrodes. We employ an uninformative prior [32] for the parameters $S_{\alpha_{UC}}$ and S_{α_C}, with a distribution that is uniform in logarithmic space, so as not to constrain the order of magnitude of the gain noises. In the case of the board-correlated noise S_{α_C}, which is poorly resolved in our data, it was necessary to add a lower limit cutoff to the prior distribution, physically motivated but conservative (see Appendix B) to ensure convergence of the Markov chain.

In Fig. 5 we also show, as black points, the projection of the actuation-only—without the background acceleration noise—contributions to acceleration noise in the

low-authority UURLA configuration. While in the three "increased actuation experiments" the measured acceleration noise is almost entirely due to actuation gain fluctuations, in the UURLA configuration actuation gain noise explains a significant, but not dominant, fraction of the measured noise in Δg across the relevant sub-mHz bandwidth. This important conclusion applies here and to the longer duration "benchmark" differential acceleration noise tests that are the published legacy of LISA Pathfinder [1,18]. In rotational acceleration, however, the actuation gain contribution would appear to explain all the measured noise in $\Delta\gamma_\phi$ at the very lowest frequencies, below 100 μHz.

The uncorrelated actuation gain noise, averaged over the eight individual electrode actuators, is resolved at all frequencies studied. While we do not resolve every individual electrode gain noise level, the four different experimental configurations and two "measurement channels" (Δg and $\Delta\gamma_\phi$) *do* allow resolution of different combinations of the uncorrelated noise in these actuators. For instance we resolve the contributions of the groups of actuators used to apply $+x$ and $-x$ forces,

$$S_{\alpha_{\mathrm{UC}+}} \equiv \frac{1}{4}(S_{\alpha_{11}} + S_{\alpha_{12}} + S_{\alpha_{21}} + S_{\alpha_{22}}),$$
$$S_{\alpha_{\mathrm{UC}-}} \equiv \frac{1}{4}(S_{\alpha_{13}} + S_{\alpha_{14}} + S_{\alpha_{23}} + S_{\alpha_{24}}). \quad (16)$$

Distributions for $S_{\alpha_{\mathrm{UC}+}}$ and $S_{\alpha_{\mathrm{UC}-}}$ are evaluated by simple summing of the MCMC chains for the individual noise parameters. The central (median) and $\pm\sigma$ values for $S_{\alpha_{\mathrm{UC}+}}$ and $S_{\alpha_{\mathrm{UC}-}}$, along with the underlying distributions, are shown in Fig. 6. In the left panel, the noise in the $+X$ actuators is clearly resolved, with $\pm\sigma$ intervals of roughly $[40, 55]$ ppm/Hz$^{1/2}$ at 121 μHz and $[6.7, 7.9]$ ppm/Hz$^{1/2}$ at 0.94 mHz. The noise in the negative actuators is smaller and more weakly resolved, with $\pm\sigma$ intervals of roughly $[10, 30]$ ppm/Hz$^{1/2}$ and $[2, 4.5]$ ppm/Hz$^{1/2}$ at the same two frequencies. The $-X$ actuator noise result is thus weakly detected, at roughly the 2σ level in noise power, with the upper limit having more relevance to our conclusions. The experiment is slightly more sensitive to the noise in the $+X$ actuators, due to the large positive forces in the "big + offset" test; nonetheless the chance statistical difference between the groups of (nominally identical) $+X$ and $-X$ actuators is significant and resolved across a large frequency range.

We note that these results are consistent with estimates from ground-measurement campaigns with the same exact actuation circuits performed years before launch. The results of those tests, which used a lock-in amplifier to measure the differential gain noise between the same electrode on the two TM—for instance $(\alpha_{21} - \alpha_{11})$—are added as additional "ground measurement" points near 0.2 mHz and 1 mHz in Fig. 6. The results are compatible,

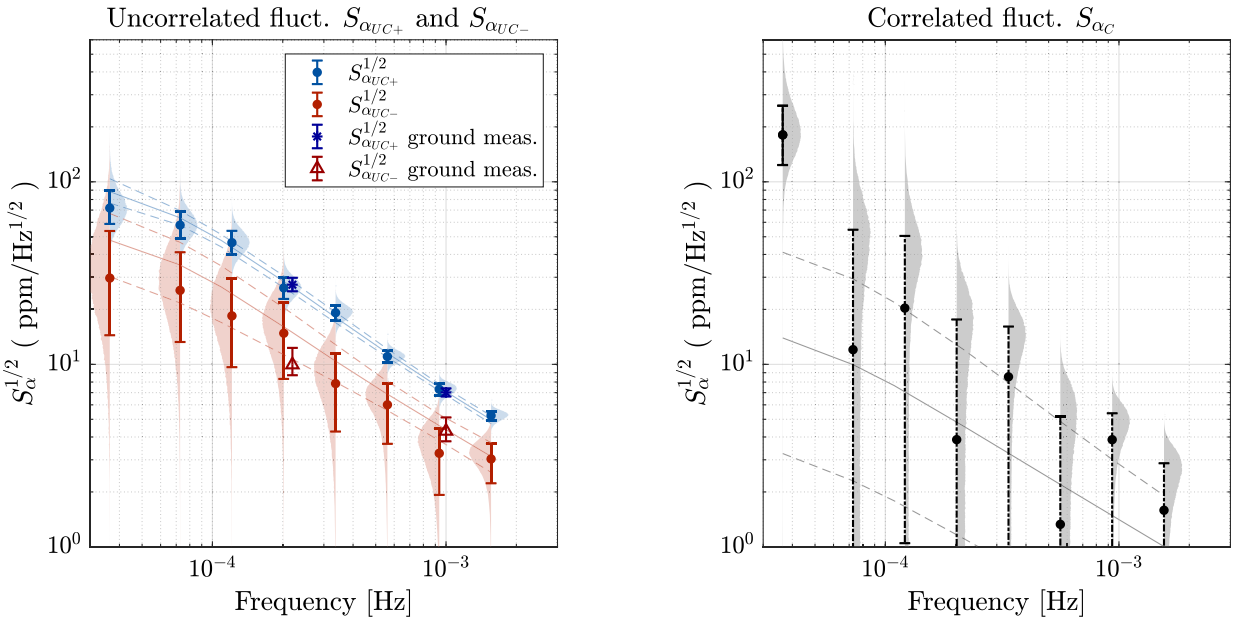

FIG. 6. Actuation gain noise results, for the uncorrelated single electrode noise in the $+X$ and $-X$ actuators at left and, at right, for the (largely unresolved) board-correlated actuation gain noise, with posterior distributions for discrete frequencies shown as shaded regions. The upper limits of all data points represent robust experimental constraints, while dashed error bars represent points for which the lower limit is largely determined by the prior assumptions. Results for a smooth, analytic frequency-dependent model fit are also shown as solid lines, with dashed lines defining the $\pm\sigma$ confidence intervals. Also shown are the results, at 0.2 mHz and 1 mHz, from a preflight ground measurement campaign with the same flight electronics.

with the specific sample of the four $+X$ actuators observed to be systematically noisier than the $-X$ circuits.

The measurement campaign is also sensitive to correlated gain fluctuations, S_{α_1} and S_{α_2}, among the two sets of four actuators used for each TM, in particular in the "big + offset" experiment with a large $+x$ force (≈ 2 nm/s^2) on both TM. However, the experimental level of correlated gain noise was low enough that the averaged board-correlated gain noise, defined as

$$S_{\alpha_C} \equiv \frac{1}{2}(S_{\alpha_1} + S_{\alpha_2}), \tag{17}$$

is essentially compatible with zero, for all but the lowest frequency analyzed, with lower limits that are strongly dependent on the prior distribution assumptions. Such points are indicated with dashed error bars in plot in the right panel in Fig. 6, while the criteria for distinguishing such points is discussed in Appendix B. The measurements do allow however robust experimental upper limits in the posterior distribution of S_{α_C}. These upper limits are virtually independent of the prior assumptions and are experimentally constraining, at a level of roughly 50 ppm/Hz$^{1/2}$ and 6 ppm/Hz$^{1/2}$ at, respectively, 121 μHz and 0.94 mHz. Inclusion of the board-correlated terms (A_i, B_i, and C_i) has little or no impact on the overall fit, and we would recover the same values for the uncorrelated noise to within 1σ in a simplified fit without the board-correlated terms. However, we know the board-correlated noise is present, at least through the voltage reference noise, and thus we keep these terms in our fit in order to place upper limits on this potentially important noise contribution.

We note also that our "nondetection" of the board-correlated gain noise is consistent with data sheet estimates for the voltage reference used in the actuation circuitry [33], for which a very rough extrapolation of the f^{-1} noise measured around 10 Hz would give several ppm/Hz$^{1/2}$ in our sub-mHz band. Additionally, no correlation of noise with platform-level thermometers is observed, and none is expected; considering data sheet values for worst-case voltage reference temperature coefficients (roughly 5 ppm/K) with typical platform-level temperature fluctuations [34], including those measured at the FEE, at 0.1 mHz at or below 0.1 K/Hz$^{1/2}$, temperature-driven voltage reference noise would be below the ppm/Hz$^{1/2}$ level (and thus not relevant at our measurement levels). In any case, our measurements indicate that board-correlated common mode gain noise is a small contributor to the LPF acceleration noise data, where applied forces were consistently below 20 pm/s^2.

An additional "raw" data curve for our actuation gain noise measurement campaign is that of the cross-spectrum between fluctuations in Δg and $\Delta\gamma_\phi$, which allows us to resolve a different combination of the uncorrelated electrode gain noises. This is shown for the four experiments at the left in Fig. 7, with solid curves representing the raw

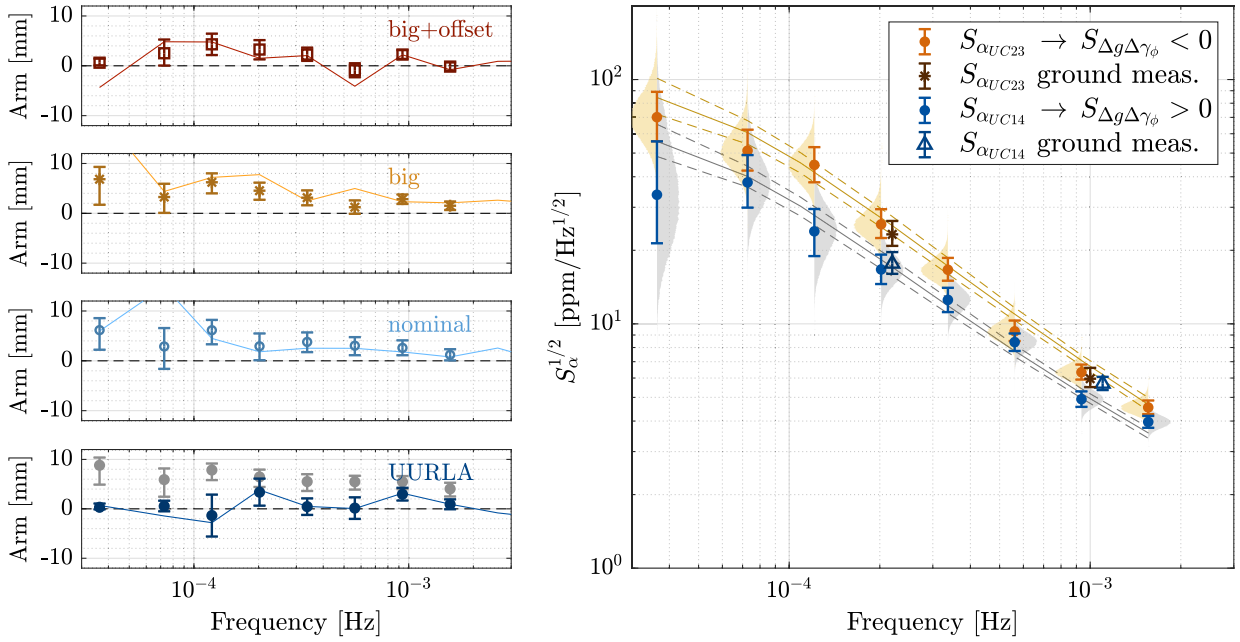

FIG. 7. At left, solid lines are raw cross spectra between Δg and $\Delta\gamma_\phi$, expressed as the effective armlength r_ϕ as defined in the text. Also shown, as discrete points with error bars, are the fit-model estimates of the effective arm (for UURLA, where actuation noise is subdominant, we also show the armlength extracted for the actuation contribution, in gray). At the right are the values of uncorrelated gain noise in the "top" electrodes 2/3 and in the "bottom" electrodes 1/4, along with estimates from on-ground electronics tests (darker points at 0.2 mHz and 1 mHz). We note that $S_{\alpha_{UC23}} > S_{\alpha_{UC14}}$ is consistent with positive armlength, r_ϕ.

periodogram cross-spectral estimates, expressed here in terms of an effective armlength defined as

$$r_\phi \equiv -\frac{I}{M}\frac{S_{\Delta g,\Delta\gamma_\phi}}{S_{\Delta g}} \approx -\frac{s^2}{6}\frac{S_{\Delta g,\Delta\gamma_\phi}}{S_{\Delta g}}, \tag{18}$$

where $s = 46$ mm is the TM sidelength. The sign convention is chosen such that a positive armlength corresponds to a predominance of force noise acting on the X faces of the TM with a force center displaced positively along the y axis. For instance, if *all* the relevant force noise were coming from actuation gain fluctuations originating in "top" electrode 2 or 3 of either TM, the translational and rotational force noise would have perfect negative correlation, with a resulting armlength $r_\phi \approx \frac{\left|\frac{\partial C_X^\star}{\partial x}\right|}{\left|\frac{\partial C_X^\star}{\partial \phi}\right|} \approx 11$ mm, half the on-center separation between adjacent electrodes on the sensor X face. If instead a "bottom" electrode 1 or 4 dominated we would find $r_\phi \approx -11$ mm, while for force noise spread equally between different X electrodes r_ϕ would tend to zero. Including the cross-spectrum data into the global fit helps break degeneracy between gain noise from electrodes $1/4$ and from electrodes $2/3$.

On the same graphs, at discrete frequencies we show the armlength extracted from the fit parameters. This is dominated by actuation, except for the low force UURLA test (where we also show both the fit-model actuation-only armlength, in gray).

We note, in both the raw armlength data and in the fit model prediction, a tendency towards positive armlengths of several mm, across the sub-mHz frequency band. With our applied forces, the typically positive values of r_ϕ indicate that electrodes $2/3$ are slightly but consistently noisier than electrodes $1/4$. This is reflected in the extracted values for the "top-bottom" groupings of the uncorrelated gain noise for the (four) electrodes $1/4$ and the group of four electrodes $2/3$,

$$\begin{aligned} S_{\alpha_{\mathrm{UC14}}} &\equiv \frac{1}{4}(S_{\alpha_{11}} + S_{\alpha_{14}} + S_{\alpha_{21}} + S_{\alpha_{24}}), \\ S_{\alpha_{\mathrm{UC23}}} &\equiv \frac{1}{4}(S_{\alpha_{12}} + S_{\alpha_{13}} + S_{\alpha_{22}} + S_{\alpha_{23}}), \end{aligned} \tag{19}$$

As with the statistical difference between the $+X$ and $-X$ electrodes, these results are consistent with the ground measurement campaign results measured years before, which also detected higher noise in the $2/3$ electrode pairs relative to electrodes $1/4$ (see discrete ground measurement points in Fig. 7).

Finally, given the observed smooth frequency dependence of the model fit—in the total acceleration noise shown in Fig. 5 but also that of the fit parameters for the different actuation gain noises, $S_{\alpha_{\mathrm{C}}}$ and $S_{\alpha_{\mathrm{UC}}}$ and the groups $S_{\alpha_{\mathrm{UC+}}}/S_{\alpha_{\mathrm{UC-}}}$ (Fig. 6) and $S_{\alpha_{\mathrm{UC14}}}/S_{\alpha_{\mathrm{UC23}}}$ (Fig. 7)—we also perform a fit with an analytical model of the frequency dependence of the actuation noise PSD, with f^{-1} and $\frac{1}{f^2+f_{3dB}^2}$ terms. These are shown as colored bands in Figs. 5 and 6. This analytical frequency-dependence does not represent a physically unique model but is chosen empirically based on the results emerging from the analysis performed at discrete frequencies, in order to allow a simple projection to other experiments at arbitrary intermediate frequencies.

The f_{3dB} term is included to describe the observed flattening of the PSD at low frequencies, with an extracted roll-off frequency of 55 ± 15 μHz. While this observed noise saturation is only slightly incompatible with a simple f^{-2}, it does indicate that there is no dramatic noise increase just below the 100 μHz band. It is also worth noting that the smooth model represents a fit with many degrees of freedom; with the 110,000 s windows used in the fit, we have roughly 600 data points—four experiments with three spectrums $S_{\Delta g}$, $S_{\Delta\gamma_\phi}$, and $S_{\Delta g,\Delta\gamma_\phi}$ and roughly 50 frequency bins—and many fewer fit parameters, 26 in all. This offers some chance for a posterior predictive goodness-of-fit test [35], performed by using the model noise parameters to predict the distribution of the Welch periodogram spectral estimates in a relatively short—in this case 2 or 3 110,000 s window—measurements. For each of the four experiments, assuming stationary Gaussian noise and an accurate model, we would expect to find 68.3% of the periodograms values in the $\pm\sigma$ interval of our model. For the four experimental runs, we find 59%, 67%, 75% and 70% of the points falling in the $\pm\sigma$ interval for, respectively, "UURLA," "nominal," "big" and "big + offset." While we do not associate the frequency-dependent fit with a rigorous physically motivated model, this goodness-of-fit indicator, in addition to the observed smoothness of the extracted noise parameters, shows consistency between the experimental data and the parametric actuation noise model considering Gaussian, stationary noise.

IV. IN-BAND VOLTAGE FLUCTUATIONS: NOISE MODEL AND EXPERIMENTAL RESULTS WITH CHARGED TM

In-band additive noise in the actuation voltages, described as $v_j(t)$ for electrode j in Eq. (7), couple to the mean TM potential, V_{TM}, related mostly to the accumulated TM charge—see line 2 of Eqs. (A4) and (A17) of Appendix A—and to the residual DC biases on the electrodes [line 3 in Eq. (A4)]. The TM charge, through the mean TM potential V_{TM}, is coupled to the average stray field, described by the translational potential difference Δ_x by (see Appendix A or Ref. [21])

$$F = -V_{\mathrm{TM}}\left|\frac{\partial C_X}{\partial x}\right|\Delta_x, \tag{20}$$

with a similar expression for the angular acceleration in terms of the rotational potential imbalance, Δ_ϕ, that couples to TM charge.

These effective differential potentials that couple to TM charge are normalized to a single X electrode capacitance, such that an additive offset in the actuation output voltage v_j, applied homogeneously across each X electrode, contributes in simple fashion to Δ_x and Δ_ϕ,

$$\begin{aligned}\Delta_x^{\mathrm{ACT}} &= v_1 + v_2 - v_3 - v_4,\\ \Delta_\phi^{\mathrm{ACT}} &= v_1 - v_2 + v_3 - v_4,\end{aligned} \tag{21}$$

for a given TM, with electrode numbering again as in Fig. 1. While noise in Δ_x and Δ_ϕ includes possible contributions from intrinsic patch-field potentials on the gold TM and electrode housing surfaces, we can interpret the measured noise levels as an upper limit of the contribution from the actuation voltages (and will comment on this hypothesis shortly).

Limiting acceleration noise from this interaction was achieved in LPF by intermittently discharging the TM, with UV illumination [16], at intervals of 1–3 weeks. With typical environmental charging approximately +25 elementary charges per second [36], the TM potential drifted away from neutral by as much as $V_{\mathrm{TM}} \approx 100$ mV [36], with a residual sensitivity to noise in Δ_x via Eq. (20). The DC value of Δ_x was measured via the change in force on the TM with a step change in TM charge [23] and then nulled by application of DC actuation voltages, thus minimizing the force noise arising from TM charge fluctuations. These were measured to be Poissonian with an effective single-charge event rate of roughly 1200/s [23] (the net charge rate of +25/s reflects a slight imbalance between a larger number of events changing the TM charge in both positive and negative directions). The residual interaction of the noisy actuation voltages v_j with the local stray DC biases can not in general be cancelled and remained a potentially relevant force noise source.

A dedicated experiment with a highly charged TM allowed quantification of the noise in Δ_x and Δ_ϕ, and thus to the stray "in-band" noise in the actuation voltages, v_j. A preliminary analysis of these tests was presented in Ref. [23]. Two new elements merit revisiting this experiment in the analysis presented here:

(i) We calculate and subtract the effect of a deterministic roundoff error in the average actuation voltage due to inaccuracies in the audio frequency actuation waveforms. This error, closely tied to the actuation force inaccuracy described in Ref. [26], introduces a noisy voltage offset varying with the commanded control forces (x) and torques (ϕ). We subtract the calculated contribution to the TM acceleration to quantify the underlying stochastic voltage noise, which is thus slightly but significantly below that originally estimated in Ref. [23].

(ii) We have added analysis of the measured differential TM angular acceleration, $\Delta\gamma_\phi$, in addition to Δg. This allows measurement of a second combination of electrode actuation voltage noise and allows assessment of correlations in the voltage noise between different channels.

The measurements were performed from May 1—May 4 in 2016, first with the two TM nearly neutral—V_{TM} of −16 mV and −24 mV for, respectively, TM1 and 2—and then with the TM charged, to roughly −1.066 V and −1.058 V. The analyzed periods for the two experiments have durations of 39 hours and 59 hours, respectively. The measured acceleration noise levels are shown in Fig. 8. A clear increase in the acceleration noise is measured in both Δg and $\Delta\gamma_\phi$, which we can attribute to noise in the relevant stray voltage fields Δ_x and Δ_ϕ in the two TM.

The increase in TM acceleration noise can be translated into an effective voltage noise, considering the differential TM accelerations Δg and $\Delta\gamma_\phi$ following the single TM treatment above [Eq. (20)]:

$$\begin{aligned}\delta\Delta g &= -\frac{1}{M}\left|\frac{\partial C_X}{\partial x}\right|[V_{\mathrm{TM2}}\delta\Delta_{x_2} - V_{\mathrm{TM1}}\delta\Delta_{x_1}]\\ &\approx -\frac{1}{M}\left|\frac{\partial C_X}{\partial x}\right|V_{\mathrm{TM}}\delta\Delta(\Delta_x),\\ \delta\Delta\gamma_\phi &\approx -\frac{1}{I}\left|\frac{\partial C_X}{\partial \phi}\right|V_{\mathrm{TM}}\delta\Delta(\Delta_\phi),\end{aligned} \tag{22}$$

with the approximation $V_{\mathrm{TM1}} \approx V_{\mathrm{TM2}} \equiv V_{\mathrm{TM}}$ valid in these experiments with the two TM each charged to roughly 1 V. Here, Δg is sensitive to the difference in the relevant coupling potential $\Delta(\Delta_x) \equiv \Delta_{x_2} - \Delta_{x_1}$ and similar for the rotational acceleration $\Delta\gamma_\phi$ in terms of the differential rotational coupling potential, $\Delta(\Delta_\phi)$. This results in acceleration noise given by

$$\begin{aligned}S_{\Delta g} &= S_{\Delta g}^{BGND} + \left(\frac{V_{\mathrm{TM}}\frac{\partial C_X}{\partial x}}{M}\right)^2 S_{\Delta(\Delta_x)},\\ S_{\Delta\gamma_\phi} &= S_{\Delta\gamma_\phi}^{BGND} + \left(\frac{V_{\mathrm{TM}}\frac{\partial C_X}{\partial \phi}}{I}\right)^2 S_{\Delta(\Delta_\phi)}.\end{aligned} \tag{23}$$

We perform independent analyses of Δg and $\Delta\gamma_\phi$ to obtain $S_{\Delta(\Delta_x)}$ and $S_{\Delta(\Delta_\phi)}$. In both cases using both a single frequency analysis and a smooth frequency dependence, chosen empirically to include f^{-1} and f^{-2} terms for both $S_{\Delta(\Delta_x)}$ and $S_{\Delta(\Delta_\phi)}$, with the observed data consistent with a f^{-1} dependence except perhaps below 100 μHz where the f^{-2} contribution could become relevant. The results of this

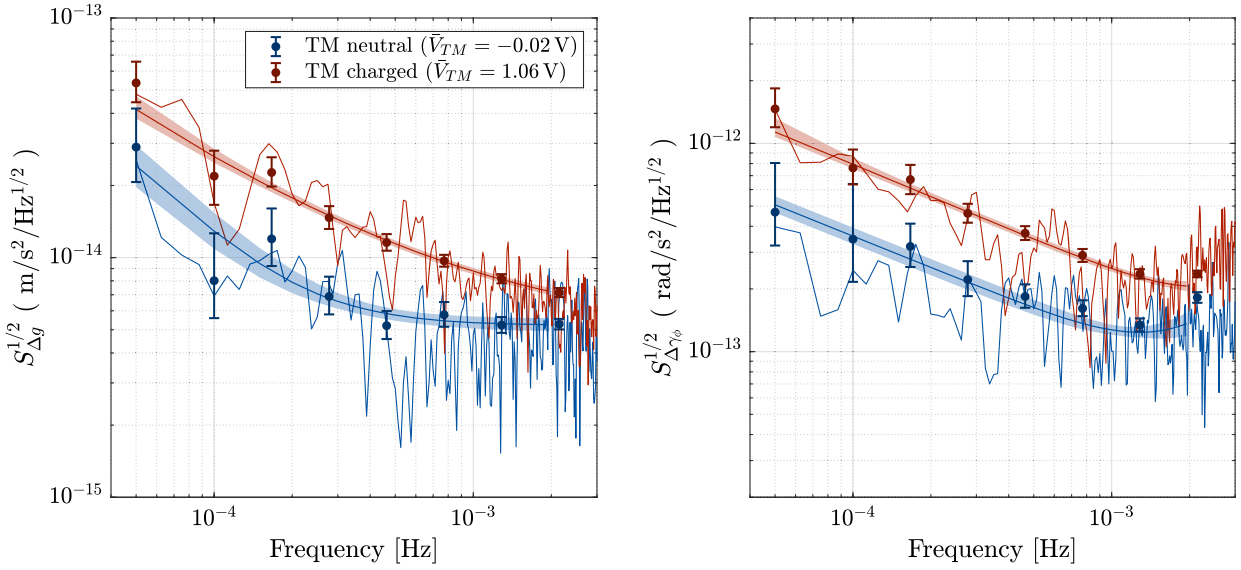

FIG. 8. Noise in the differential acceleration (translational Δg and rotational $\Delta\gamma_\phi$) measured with the two LPF TM charged to roughly -1.06 V and with the TM nearly neutral. Results of model fits to the joint Δg and $\Delta\gamma_\phi$ dataset are shown, at single frequencies and for an analytic model with f^{-1} and f^{-2} frequency dependence, respectively, as single points with error bars and colored bands.

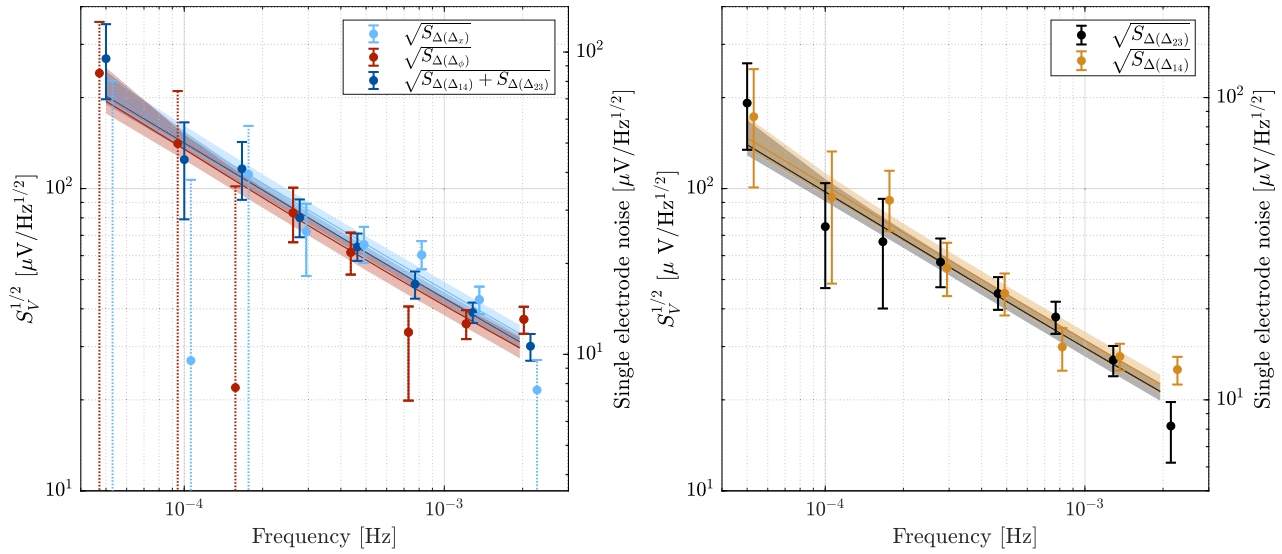

FIG. 9. On the left, noise in the actuation voltage combinations, $\Delta(\Delta_x)$ and $\Delta(\Delta_\phi)$ (points and colored bands in light blue and red), coupling to, respectively, translational and rotational acceleration noise in the individual Δg and $\Delta\gamma_\phi$ datasets in Fig. 8. The combinations $\Delta(\Delta_{12})$ and $\Delta(\Delta_{23})$, from the joint, correlated analysis of the Δg and $\Delta\gamma_\phi$, are shown individually on the right and summed on the left (dark blue points). In both cases, colored bands illustrate the result of the model with analytic f^{-1} and f^{-2} frequency dependence. For both graphs, a righthand axis indicates the effective single electrode voltage noise inferred from the noise in the various combinations (all of these estimates are mutually consistent).

analysis are shown in Fig. 9, with the frequency-smooth fits to the acceleration noise model overlayed in Fig. 8. We note that the independent analyses of the translational and rotational noise makes no assumptions about correlations between voltage fluctuations on the different electrodes, and we will comment on this shortly.

The smooth fit for $S_{\Delta(\Delta_x)}$ around 0.1 mHz has a $\pm\sigma$ interval of roughly $[135, 165]$ μV/Hz$^{1/2}$, compared to $[225, 320]$ μV/Hz$^{1/2}$ reported in Ref. [23].[2] This reduction is related to the deterministic subtraction of the actuation

[2]The result of $[160, 200]$ μV/Hz$^{1/2}$ in Ref. [23] was for S_{Δ_x} for a single TM, assuming that the two TM have uncorrelated, statistically equivalent noise in Δ_x. The differential noise in Δ_x that is truly measured, and compared here, is thus simply multiplied by a factor two in power.

voltage roundoff error. The results for $S_{\Delta(\Delta_\phi)}$ are similar to those for Δ_x, with a $\pm\sigma$ interval $[120, 150]\ \mu\mathrm{V/Hz}^{1/2}$ at 0.1 mHz.

We observe that $S_{\Delta(\Delta_x)} \approx S_{\Delta(\Delta_\phi)}$ across the frequency band. If there were an important correlated fluctuations between actuation voltages on different electrodes, these could add or subtract differently in the combinations [see Eq. (21)] coupling into force and torque, resulting in different noise levels in Δ_x and Δ_ϕ. The absence of such a noise asymmetry is at least consistent with uncorrelated voltage fluctuations.

Additionally, $S_{\Delta(\Delta_x)} \approx S_{\Delta(\Delta_\phi)}$ suggests that actuation voltage noise—rather than fluctuations of patch potentials on the gold TM and electrode surfaces—are dominating the interaction with the charged TM. If patch-field effects were dominant, one would expect $S_{\Delta(\Delta_\phi)} > S_{\Delta(\Delta_x)}$, by perhaps a factor 2–3. This is expected first because the rotational combination Δ_ϕ includes significant contributions from the electrode housing X and Y surfaces while Δ_x mainly involves just the X surfaces. Second, the Y electrode housing surfaces on the Y faces are closer ($d_y = 2.9$ mm while $d_x = 4$ mm, with the relevant capacitance derivatives scaling as d^{-2}). Thus the rough equivalence $S_{\Delta(\Delta_x)} \approx S_{\Delta(\Delta_\phi)}$ is consistent with actuation voltage fluctuations.

In the hypothesis that coupling to TM charge is dominated by uncorrelated in-band additive noise in the actuation voltages, we can further dissect the contribution of stray actuation voltage to the measured differential TM accelerations. Specifically,

$$\begin{aligned}\Delta(\Delta_x^{\mathrm{ACT}}) &\equiv \Delta_{x_2}^{\mathrm{ACT}} - \Delta_{x_1}^{\mathrm{ACT}} = \Delta(\Delta_{14}) + \Delta(\Delta_{23}),\\ \Delta(\Delta_\phi^{\mathrm{ACT}}) &\equiv \Delta_{\phi_2}^{\mathrm{ACT}} - \Delta_{\phi_1}^{\mathrm{ACT}} = \Delta(\Delta_{14}) - \Delta(\Delta_{23}),\end{aligned} \tag{24}$$

where $\Delta(\Delta_{14})$ and $\Delta(\Delta_{23})$ are each 4-electrode actuation voltage noise differences,

$$\begin{aligned}\Delta(\Delta_{14}) &\equiv v_{21} - v_{24} - v_{11} + v_{14},\\ \Delta(\Delta_{23}) &\equiv v_{22} - v_{23} - v_{12} + v_{13},\end{aligned} \tag{25}$$

with v_{ij} for the stray additive actuation voltage on electrode j of the LPF TM i. The sum and difference of the voltage combinations $\Delta(\Delta_{14})$ and $\Delta(\Delta_{23})$ thus couple into differential translational and rotational acceleration Δg and $\Delta\gamma_\phi$. In the hypothesis that the noise in $\Delta(\Delta_{14})$ and $\Delta(\Delta_{23})$ are uncorrelated, we can see from Eqs. (22) and (24) that the noise in Δg and $\Delta\gamma_\phi$ will each be proportional to the sum, $(S_{\Delta(\Delta_{14})} + S_{\Delta(\Delta_{23})})$, while the cross-spectrum $S_{\Delta g,\Delta\gamma_\phi}$ will be proportional to the difference, $(S_{\Delta(\Delta_{14})} - S_{\Delta(\Delta_{23})})$. Fitting to this model, including $\{S_{\Delta g}, S_{\Delta\gamma_\phi}, S_{\Delta g,\Delta\gamma_\phi}\}$ in a single analysis, we obtain estimates for $S_{\Delta(\Delta_{14})}$ and $S_{\Delta(\Delta_{23})}$ (at right in Fig. 9). Consistent with a model of uncorrelated $\Delta(\Delta_{14})$ and $\Delta(\Delta_{23})$, their sum is compatible with the individual analyses for $S_{\Delta(\Delta_x)}$ and $S_{\Delta(\Delta_\phi)}$ (shown on the left in Fig. 9).

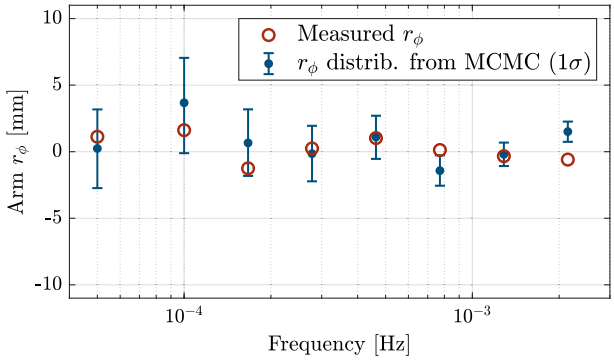

FIG. 10. Effective armlength r_ϕ, based on cross-spectral density $S_{\Delta g,\Delta\gamma_\phi}$ as defined in Eq. (18), in the charged TM experiment, raw (red) and reconstructed with $\pm\sigma$ error bars from the MCMC fit (blue). The data are consistent with uncorrelated translational and rotational acceleration noise.

Additionally, the cross-correlation between acceleration noise Δg and $\Delta\gamma_\phi$ is compatible with zero across the frequency band studied (Fig. 10). If the increase in TM acceleration noise were dominated by a single "bad" noisy electrode, we would expect a full force/torque correlation—with armlength $r_\phi \approx \pm 11$ mm, depending on the electrode—but that is not observed here. Null cross-correlation is consistent with $S_{\Delta(\Delta_{14})} \approx S_{\Delta(\Delta_{23})}$, indicating that the summed noise in the two groups of 4 electrodes [Eq. (25)] are statistically equivalent at our level of measurement resolution.

All of these observations are consistent with coupling of charge into TM acceleration via uncorrelated actuation voltage noise, roughly with the same PSD in the eight relevant X electrodes for the two TM. This is the simplest and perhaps most reasonable model—considering the eight nominally identical actuation circuits—though not the only possible explanation of the measured data. In this model, the single electrode actuation voltage noise, $S_v \approx \frac{1}{4}S_{\Delta(\Delta_{14})} \approx \frac{1}{4}S_{\Delta(\Delta_{23})} \approx \frac{1}{8}S_{\Delta(\Delta_x)} \approx \frac{1}{8}S_{\Delta(\Delta_\phi)}$ and shown with the righthand axes in both plots of Fig. 9, is roughly $50\ \mu\mathrm{V/Hz}^{1/2}$ at 0.1 mHz and $15\ \mu\mathrm{V/Hz}^{1/2}$ at 1 mHz. While we do not have detailed low-frequency ground data with which to compare, the results at 1 mHz are roughly in line with the results of shorter preflight measurements.

We note that the observed effective single electrode voltage noise will contribute to the noise in measurements of the TM charge, performed as in LPF [23,36] with a modulated voltage applied to the four X electrodes. This technique essentially detects the potential difference between the TM and the average DC potential of the modulating electrodes [20]. However, the measured in-band actuation noise presented here is too small, by slightly more than an order of magnitude, to explain the measured

TM charge fluctuations, equivalent to TM potential fluctuations of order 300 $\mu V/Hz^{1/2}$ at 0.1 mHz [23], which instead remain compatible with a cosmic ray Poissonian charge noise of roughly 1200/s. This conclusion would remain valid even without the "correction" for the digitazion roundoff error mentioned above.

V. PROJECTIONS OF ACCELERATION NOISE FROM ACTUATION IN LPF AND LISA

A projection of the actuation gain and in-band voltage noise model and experimental parameters for the long (14 day) LPF benchmark differential acceleration noise measurement from February 2017 [18] is shown, with $\pm\sigma$ uncertainty bands, in Fig. 11. Actuation gain noise is calculated using the models [Eq. (B2)] and Markov chain parameter values of Sec. III, considering the A and B coefficients [Eq. (B1)] as calculated from the commanded actuation force telemetry for the February 2017 run. The same is done for the in-band voltage noise mixing with the TM charge, using the model of Eq. (23) with the noise parameters from the MCMC analysis of the charged TM experiment (Sec. IV) and the root mean square (rms) TM charge values estimated from charge measurements before and after the February 2017 runs.

The actuation gain fluctuations were a sizable but not dominant contribution to the main science measurement of Δg; at 0.1 mHz this noise source is 3.5–5 $fm/s^2/Hz^{1/2}$ or roughly 20–40% of the total measured acceleration noise power. This contribution was limited by the exceptionally accurate gravitational (DC force) balancing along the LPF x axis, which allowed lowering the actuation force authority to 26 pm/s^2 for the mission science operations; had a larger DC force imbalance imposed the use of the nominal authority (1140 pm/s^2), the acceleration noise due to actuation would have dominated the LPF noise floor and pushed it to the 60–70 fm/s^2 level at 0.1 mHz as in the "nominal" actuation test (Table I and light blue data in Fig. 5). The in-band additive voltage noise is a small contributor, roughly 1 $fm/s^2/Hz^{1/2}$ at 0.1 mHz, at least with the relatively low, roughly 40 mV, rms TM potential in this run.

We can also project these results for actuation noise to the LISA mission, shown in Fig. 12. LISA requires no TM x-axis actuation forces, with the spacecraft drag-free controlled to follow the TM along this critical constellation interferometry axis. With $g_c = 0$ in Eq. (11), there is no coupling to fully correlated gain fluctuations of the four X electrode channels ($A_i = 0$). However, the ϕ torque actuation with uncorrelated gain fluctuations in the four X actuation circuits will produce acceleration noise, with nonzero coefficients A_{ij},

$$\begin{aligned} S_g^{\mathrm{ACT}} &= R_\phi^{\star 2}(\gamma_{\phi_c}^2 + \gamma_{\phi_0}^2) S_{\alpha_{\mathrm{UC}}}(f) \\ &\approx [3.5\ \mathrm{fm/s^2/Hz^{1/2}}]^2 \times \left[\frac{\gamma_{\phi_c}^2 + \gamma_{\phi_0}^2}{(1^2 + 1.5^2)\ (\mathrm{nrad/s^2})}\right]^2 \\ &\quad \times \frac{S_{\alpha_{\mathrm{UC}}}}{(50\ \mathrm{ppm/Hz^{1/2}})^2}, \end{aligned} \tag{26}$$

where 50 $ppm/Hz^{1/2}$ is a reference level at 0.1 mHz from the measurements presented in Sec. III for the (noisier)

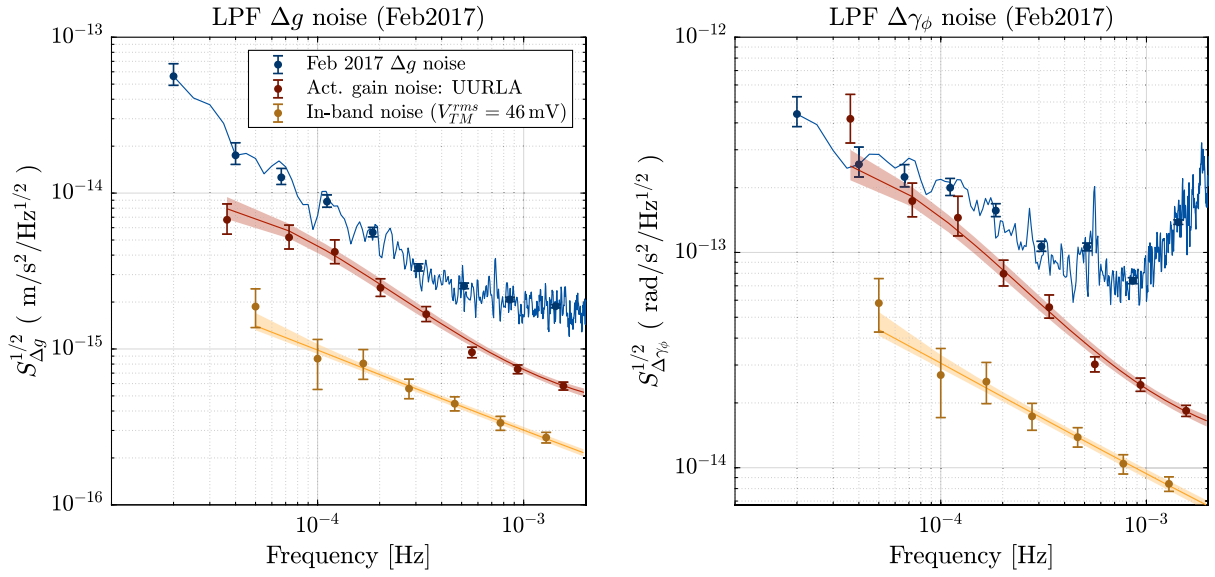

FIG. 11. Differential acceleration noise measured by LPF across roughly 340 hours in February 2017 [18], shown with projections of the noise contributions from actuation gain fluctuations and in-band additive voltage noise. We note that the force /torque authorities ($\gamma_{\phi_{10}}, g_{20}, \gamma_{\phi_{20}}$) were identical to those for UURLA in the actuation noise experiment (Table I) while the average applied forces were similar ($\gamma_{\phi_{1c}} = -970$ prad/s^2, $g_{2c} = +5$ pm/s^2, and $\gamma_{\phi_{2c}} = +150$ prad/s^2). Time-averaged rms values for the TM potential were each found to be roughly 40 mV based on TM charge measurements performed before and after the long measurement.

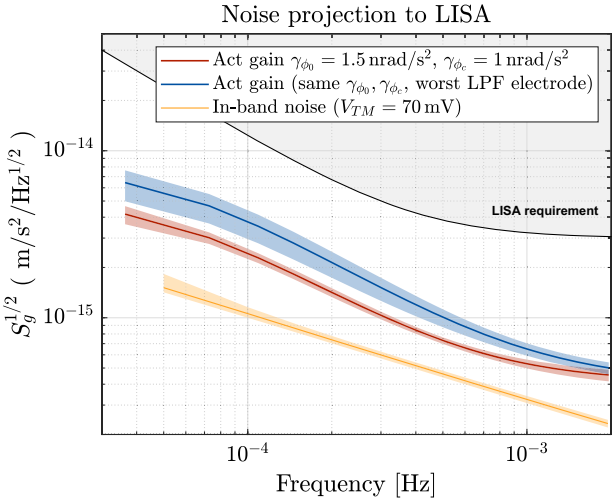

FIG. 12. Projections of actuation noise contributions to LISA x axis TM acceleration noise, from actuation gain noise and in-band voltage noise as estimated in this paper. The LISA conditions assume ϕ actuation authority $\gamma_{\phi_0} = 1.5$ nrad/s^2 and commanded torque $\gamma_{\phi_c} = 1.0$ nrad/s^2, using the averaged gain noise measured here and, as a worst case, the values for the worst LPF electrode performance (TM1, electrode 2) assigned to all 4 X electrode actuators. For the coupling to in-band voltage noise, the TM potential is assumed to be at the discharge threshold of 70 mV.

$X+$ LPF actuators. The reference torque levels consider compensation of a ϕ DC angular acceleration of 1 nrad/s^2, with an actuator torque authority of 1.5 nrad/s^2, allowing some headroom for controller dynamics. This can be considered a realistic gravitational balance requirement on board a LISA spacecraft, based on the LPF experience. Indeed the needed applied ϕ torques on the two LPF TM, $\gamma_{\phi_{1c}}$ and $\gamma_{\phi_{2c}}$ in Table I, which were within 100 prad/s^2 of, respectively, -1000 prad/s^2 and $+150$ prad/s^2 over the course of the mission. These are each compatible, magnitude and sign, with the preflight estimates from the gravitational model to within 200 prad/s^2[3] and further gravitational compensation could have reduced the residual values further, well within the 1000 prad/s^2 limit proposed for LISA.

For the coupling of the actuation "in-band" noise to TM charge, we would have

$$\begin{aligned} S_g^q &\approx 4\left[\frac{1}{M}\frac{\partial C_X}{\partial x}\frac{q}{C_T}\right]^2 S_{v_n}(f) \\ &\approx [1\ \mathrm{fm/s^2/Hz^{1/2}}]^2 \times \left(\frac{q}{1.5\times 10^7 e}\right)^2 \\ &\quad \times \frac{S_{v_n}}{(50\ \mu\mathrm{V/Hz^{1/2}})^2}. \end{aligned} \tag{27}$$

[3]Compare with values for angular accelerations α_ϕ in Table A1 of Ref. [4].

In Fig. 12 we use a worst case TM charge of ± 15 million elementary charges (± 70 mV TM potential). For the typical LPF charging conditions [23] of $+25$ e/s, maintaining the TM charge in this interval would require discharging roughly every two weeks, with up to twice this rate depending on solar cycle variations [19,37]. Alternatively the TM charge can be held near zero with a continuous UV illumination of the TM, which was also demonstrated in a dedicated experiment by LPF [38] and is under study for LISA [39]. The in-band voltage fluctuations will introduce force noise of similar magnitude in the interaction with the average stray biases on each electrode, considered to be of order 20–50 mV rms based on measurements in flight with LPF and on ground with various GRS prototypes [21,23].

VI. CONCLUSIONS

LISA Pathfinder allowed demonstration of the key electrostatic actuation system needed for LISA, demonstrating its compatibility with differential acceleration measurements at the 10 fm/s^2/Hz$^{1/2}$ level at 0.1 mHz, as needed for high precision measurement of tidal accelerations from supermassive black holes in the LISA observatory. The conditions of LISA Pathfinder were actually slightly more challenging than those envisioned for LISA from the standpoint of applied forces, requiring x-axis force actuation that will not be needed in LISA.

In the on-orbit measurement campaign presented in Sec. III, we successfully detect acceleration noise from actuation gain fluctuations, compatible with a simple parametric gain model with noise scaling with the applied forces and a clear detection of a dominant role, in LPF, of force noise from uncorrelated fluctuations in the different electrode actuation circuits rather than board-correlated actuator gain noise, as would instead result from a noisy DAC reference voltage. Measured levels of gain noise were in agreement with the limited ground testing measurements performed and used in LPF noise predictions [3], even detecting the same chance variations in the noise levels for different groups of the nominally identical eight relevant electrode actuator circuits.

As shown in Fig. 11, actuation gain noise was an important but not dominant source of noise in LPF, responsible for roughly 20–40% of the noise power for Δg in the 0.1 mHz band. Our measurements clearly resolved the actuation gain fluctuations by increasing, compatibly with dynamic control constraints, the applied actuation forces well beyond their needed levels. Similarly, in-band low-frequency voltage noise was indeed measurable, but only after increasing the TM charge by more than a factor of 10 beyond the typically used values.

The contribution of actuator gain noise in the LPF benchmark acceleration noise measurements was kept at a minimal level because the gravitational balance was considerably better than the values that were budgeted,

or 650 $\mathrm{pm/s^2}$ [3] or even predicted as uncertainties in the preflight gravitational models [4], order ± 300 $\mathrm{pm/s^2}$. The residual x-axis acceleration noise contribution from the applied actuation forces was determined roughly in equal measure from ϕ torques in addition to the TM2 applied x forces.

Additional LPF differential acceleration tests were also performed in an open-loop free-fall mode, without any TM2 x force actuation except during brief control kicks that were excised from the data in postprocessing. Though originally designed to improve the LPF noise by removing a dominant actuation contribution [3], the test results showed no measurable difference [40]; due to the better than expected gravitational balancing and consequent lower-force levels, x-axis actuation noise was small enough that its removal produced essentially no resolvable improvement in the noise.

The remaining low-frequency LPF noise is subject of ongoing research and will be addressed in a future publication [41]. We cannot exclude that some of the remaining excess low frequency acceleration noise, in February 2017 and in the other low-force, low-noise [1,18] runs, comes from the actuation system by another mechanism *not covered* by our gain noise model here. To be quantitatively relevant, such an effect would have to scale "more slowly" with the applied forces than for gain noise, which scales as $\delta F \propto F$ and thus $S_g \propto g_c^2$. An additive voltage noise with frequency dependence around the actuation carrier frequencies could give an effective low frequency amplitude-modulation noise, with a PSD that scales linearly with applied force authorities [such as in Eq. (13)]. Such an effect was detected with the actuation digitization accuracy issue mentioned earlier [26], though the error is believed to have been successfully understood and corrected. This deterministic correction is of order 10 μV rms out of a total LSB of 153 μV; a possible residual inaccuracy, an effective DAC nonlinearity, of $1-2$ μV in the calculation of the true applied amplitudes, would be sufficient to account for the observed excess noise in the 0.1–1 mHz band. Such a level of error can not be ruled out by other in-flight measurements, such as the calibration-tone experiment (Fig. 3) or the gain-noise measurement campaign presented in Sec. III. We are currently investigating, with both analysis and measurement on available LPF-prototype FEE models, if such a residual error could be compatible with the LPF actuation electronics.

Mixing of actuator in-band voltage noise with TM charge and other stray DC potentials is shown to have a small impact in LPF or, assuming appropriate charge management, in LISA, with the current measurements establishing a lower noise level with respect to earlier LPF results [23] and confirming a scenario of stray field fluctuations dominated by uncorrelated additive actuation circuitry noise acting on individual electrodes. However, even at the lower noise level measured here, stray electrostatics still drive the use of audio frequency carriers to apply DC or slowly varying electrostatic forces. A "DC drive" electrostatic actuation for ϕ torques at the LISA-required 1.5 $\mathrm{nrad/s^2}$ level would require applied voltages up to 0.7 V, an order of magnitude larger than the DC potential differences arising from the levels proposed for TM charge or stray DC biases. With 50 $\mu\mathrm{V/Hz^{1/2}}$ electrode voltage noise at 0.1 Hz, this would give 7 $\mathrm{fm/s^2/Hz^{1/2}}$ and thus consume nearly half the entire LISA acceleration noise budget.

The unique potential of the LPF Δg dataset has been recognized beyond its value as a benchmark for LISA free-fall as a small force probe for, among other questions, setting upper limits on wave function collapse models [42] and searching for ultralight dark matter [43]. Our current article is the first to use the high precision LPF *differential angular acceleration* measurement, $\Delta\gamma_\phi$, and the sensitivity reached merits a comment. While rotational acceleration noise is not intrinsically essential to the LISA low-frequency gravitational wave sensitivity, the LPF $\Delta\gamma_\phi$, including an interferometric readout with sub-$\mathrm{nrad/Hz^{1/2}}$ resolution [10], proved invaluble in this investigation of actuator force noise, allowing us to disentangle effects that would have had degenerate signatures in the Δg translational channel alone. The differential torque resolution reached in the low-force UURLA configuration (see the right-hand plots in Figs. 5 or 11) is below 0.1 $\mathrm{fNm/Hz^{1/2}}$ across a decade of frequency (0.15–1.5 mHz), an improvement of nearly an order of magnitude beyond the best measurements on ground using a single, hollow LISA TM inside a prototype electrode housing with fused silica suspension torsion pendulums [44,45]. Actuation gain noise is a big portion of the LPF differential angular acceleration noise, responsible for roughly half the noise power at 0.1 mHz and an even larger fraction at lower frequencies. The clean LPF system and environment on orbit thus also realized an improved fiberless torsion pendulum that proved essential for these tests of critical hardware for LISA, as well as for the overall understanding of low-frequency force noise in the experimental challenge of free-falling reference test masses.

ACKNOWLEDGMENTS

This work has been made possible by the LISA Pathfinder mission, which is part of the space-science program of the European Space Agency. We acknowledge the work of the prime contractor for LPF and for the "LISA Technology Package," Airbus Defense and Space, for the industrial implementation of the electrostatic actuation suspension as part of the overall DFACS dynamic control under their responsibility. The Italian contribution has been supported by Istituto Nazionale di Fisica Nucleare (INFN) and Agenzia Spaziale Italiana (ASI), Project No. 2017-29-H.1-2020 "Attività per la fase A della missione LISA."

The UK groups wish to acknowledge support from the United Kingdom Space Agency (UKSA), the Scottish Universities Physics Alliance (SUPA), the University of Glasgow, the University of Birmingham, and Imperial College London. The Swiss contribution acknowledges the support of the Swiss Space Office via the PRODEX Programme of ESA, the support of the ETH Research Grant No. ETH-05 16-2 and the support of the Swiss National Science Foundation (Projects No. 162449 and No. 185051). The Albert Einstein Institute acknowledges the support of the German Space Agency, DLR. The work is supported by the Federal Ministry for Economic Affairs and Energy based on a resolution of the German Bundestag (No. FKZ 50OQ0501, No. FKZ 50OQ1601, and No. FKZ 50OQ1801). J. I. T. and J. S. acknowledge the support of the U.S. National Aeronautics and Space Administration (NASA). Spanish contribution has been supported by Contracts No. AYA2010-15709 (Ministerio de Ciencia e Innovación, MICINN), No. ESP2013-47637-P, No. ESP2015-67234-P, No. ESP2017-90084-P (Ministerio de Asuntos Económicos y Transformación Digital, MINECO), and No. PID2019–106515GB-I00 (MICINN). Support from AGAUR (Generalitat de Catalunya) Contract No. 2017-SGR-1469 is also acknowledged. M. N. acknowledges support from Fundacion General CSIC (Programa ComFuturo). F. R. acknowledges an FPI contract from MINECO. The French contribution has been supported by the CNES (Accord Specific de Project No. CNES 1316634/CNRS 103747), the CNRS, the Observatoire de Paris and the University Paris-Diderot. E. P. and H. I. would also like to acknowledge the financial support of the UnivEarthS Labex program at Sorbonne Paris Cité (No. ANR-10-LABX-0023 and No. ANR-11-IDEX-0005-02). N. K. would like to thank for the support from the CNES Fellowship.

APPENDIX A: MODEL OF ELECTROSTATIC FORCES AND FORCE NOISE

This section summarizes the electrostatic model used, which is then applied to describe both the nominal actuation design and the two main acceleration noise sources addressed by this paper.

We use the electrostatic force model developed in Refs. [21,25,46], considering the TM and surrounding sensor (S) surfaces as a patchwork of equipotential domains. The resulting instantaneous force on the TM along the sensor x axis is given by

$$F_x = \frac{1}{2}\sum_{m,n<m}\frac{\partial C_{nm}}{\partial x}(V_m - V_n)^2, \tag{A1}$$

where C_{nm} is the capacitive element between surface domains m and n.

For actuation/sensing electrode j, we can consider the potential on domain $m(j)$ as a sum of the actuation voltage V_j applied homogeneously to the entire electrode and a local "patch potential" δV_m,

$$V_{m(j)} = V_j + \delta V_m. \tag{A2}$$

The sensor surfaces also include grounded electrode housing guard rings (H) with possible stray surface potentials, $V_{m(H)} = \delta V_m$.

For a TM domain $n(\mathrm{TM})$, we have $V_{n(\mathrm{TM})} = V_{\mathrm{TM}} + \delta V_n$, with the average TM potential given by

$$\begin{aligned} V_{\mathrm{TM}} &= \frac{q}{C_T} + \frac{\sum_{n(S)} C_{n(S)}\delta V_n}{C_T} + \frac{\sum_j C_j V_j}{C_T} \\ &= V_{\mathrm{TM0}} + V_{\mathrm{TM}}^{\mathrm{ACT}}. \end{aligned} \tag{A3}$$

In the second line we divide the equation into an intrinsic TM potential V_{TM0} from EH stray surface potentials and an induced electrostatic potential from the actuation voltages $V_{\mathrm{TM}}^{\mathrm{ACT}}$. Here $C_{n(S)}$ is the capacitance of sensor domain n to all TM domains, C_j is the total capacitance of electrode j to the TM, and $C_T \equiv \sum_{n(S)} C_{n(S)}$ is the total TM capacitance to all electrode housing surfaces.

To isolate the electrostatic force contribution from applied actuation voltages, we can consider the terms in Eq. (A1) that involve domains on the sensing/actuation electrodes. We neglect here the interaction between domains on the same electrode—for which the applied actuation voltage cancels in the potential differences in Eq. (A1)—and between domains on different electrodes, as the capacitance between these is quite small and shielded by the ground ring surfaces. Thus considering interactions between domains on actuation electrodes and those on the TM and on the grounded guard ring surfaces, we find, summing over the electrostatic domains $m(j)$ on each actuation electrode j,

$$\begin{aligned} F_x^{\mathrm{ACT}} = \sum_j \Bigg\{ &\frac{1}{2}\frac{\partial C_j^\star}{\partial x} V_j^2 + V_j \Bigg[-\frac{\partial C_j}{\partial x}(V_{\mathrm{TM0}} + V_{\mathrm{TM}}^{\mathrm{ACT}}) \\ &+ \sum_{m_j, n(TM,H)} \frac{\partial C_{m_j n}}{\partial x}(\delta V_{m_j} - \delta V_n) \Bigg] \Bigg\}. \end{aligned} \tag{A4}$$

This equation for the instantaneous electrostatic force considers the capacitive derivatives evaluated for the true TM position. We have introduced the total capacitance of an electrode to the TM and to the adjacent grounded housing, $C_j^\star \equiv \sum C_{m(j),n(TM,H)}$.

Analogous expressions govern the force and torques on the other axes. We note that, while only the four electrodes on the X faces of the EH have a significant derivative, $\frac{\partial C_j}{\partial x}$, the single TM average potential is relevant to the force on any degree of freedom, such that the third term involving

$V_{\mathrm{TM}}^{\mathrm{ACT}}$ will couple the actuation forces and torques on different axes.

1. Actuation design, nominal forces and force gradients

The guiding principles to the actuation concept proposed early in LPF development [14] follow from Eq. (A4):

(i) Exploit the quadratic dependence, $F \propto V^2$, to produce DC or slowly varying control forces with zero-mean audio-frequency voltages. The control force is the low-frequency component $\langle V_j^2 \rangle$ in the first term in Eq. (A4)—$\langle\rangle$ denoting a time average over the actuation carrier period—and thus independent of TM potential from charge q and of stray surface potentials, which enter in the second (V_{TM0}) and fourth (δV_m) terms in Eq. (A4). Forces from these uncontrolled and noisy quasi-DC potentials are spectrally shifted out of band, around the AC carrier frequencies (60–270 Hz in LPF), as is any self-mixing between the actuation carrier and low-frequency in-band actuation noise.

(ii) Reduce the coupling between d.o.f. by applying actuation voltages with symmetry such that the induced actuation potential $V_{\mathrm{TM}}^{\mathrm{ACT}}$—the third term in Eq. (A4) for x but also relevant to the actuation force on all d.o.f.—is zero, at least for a centered TM. This is done by requiring that the sum of the applied actuation voltages on the four X (or Y or Z) electrodes is zero at all times.

(iii) Further decouple the d.o.f. with actuation waveforms chosen to be orthogonal between different degrees of freedom. In LPF this was implemented with sinusoids at six different actuation frequencies.

(iv) Make TM control dynamics more simple and predictable, by maintaining the force gradients introduced by the actuation electrostatic fields—through the position dependence of the capacitive derivatives (first term) and the induced $V_{\mathrm{TM}}^{\mathrm{ACT}}$ (third term) independent of the commanded force and torque. How to do this will be shown shortly.

As an example of the actuation algorithm and nominal forces, torques and their gradients, we consider the x and ϕ degrees of freedom, actuated using the four X-face electrodes. We consider the following actuation scheme, generalized from Eq. (2):

$$\begin{aligned} V_{1c}(t) &= V_{1x}\chi_{1x}(t) + V_{1\phi}\chi_{1\phi}(t), \\ V_{2c}(t) &= -V_{1x}\chi_{1x}(t) + V_{2\phi}\chi_{2\phi}(t), \\ V_{3c}(t) &= +V_{2x}\chi_{2x}(t) - V_{1\phi}\chi_{1\phi}(t), \\ V_{4c}(t) &= -V_{2x}\chi_{2x}(t) - V_{2\phi}\chi_{2\phi}(t). \end{aligned} \tag{A5}$$

Each waveform χ is zero mean—for instance $\langle \chi_{1x}(t) \rangle = 0$, with sine-equivalent amplitudes such that $\langle \chi_{1x}^2 \rangle = 0.5$. Additionally, the waveforms are orthogonal between different degrees of freedom ($\langle \chi_{1x}\chi_{1\phi} \rangle = 0$ for instance), which was achieved in LPF with six different actuation frequencies for the six d.o.f.

In evaluating the capacitances relevant to the electrostatic forces, we consider an expansion to first order to the relevant displacements in the xy plane,

$$\begin{aligned} C_j &= C_{X0} \pm \frac{\partial C_X}{\partial x}x \pm \frac{\partial C_X}{\partial \phi}\phi, \\ \frac{\partial C_j}{\partial x} &= \pm\left|\frac{\partial C_X}{\partial x}\right| + \left|\frac{\partial^2 C_X}{\partial x^2}\right|x \pm \left|\frac{\partial^2 C_X}{\partial x \partial \phi}\right|\phi, \\ \frac{\partial C_j}{\partial \phi} &= \pm\left|\frac{\partial C_X}{\partial \phi}\right| + \left|\frac{\partial^2 C_X}{\partial \phi^2}\right|\phi \pm \left|\frac{\partial^2 C_X}{\partial x \partial \phi}\right|x, \end{aligned} \tag{A6}$$

with the signs ($\pm$) changing with the positions of the different electrodes.

Neglecting any stray DC fields (δV_m and q) and considering only the DC force component, considering higher-order harmonics as out of band, we obtain a force,

$$\begin{aligned} F_x = &\frac{1}{2}\left|\frac{\partial C_X^\star}{\partial x}\right|(V_{1x}^2 - V_{2x}^2) \\ &+ \frac{1}{2}\left|\frac{\partial^2 C_X^\star}{\partial x^2}\right|x[V_{1x}^2 + V_{2x}^2 + V_{1\phi}^2 + V_{2\phi}^2] \\ &- 2\frac{|\frac{\partial C_X}{\partial x}|^2}{C_T}x[V_{1\phi}^2 + V_{2\phi}^2 + V_{1\phi}V_{2\phi}\langle\chi_{1\phi}\chi_{2\phi}\rangle], \end{aligned} \tag{A7}$$

Additionally requiring that the two ϕ waveforms be "orthogonal," with $\langle \chi_{1\phi}\chi_{2\phi} \rangle = 0$—obtained using sine and cosine waveforms in LPF, see Eq. (2)—eliminates the cross-term dependent on the product $V_{1\phi} \times V_{2\phi}$. We thus obtain,

$$F_x = Mg_c - M\omega_{xx}^2 x, \tag{A8}$$

with a nominal, TM centered, applied force per unit mass g_c and a force gradient described by stiffness, ω_{xx}^2,

$$\begin{aligned} g_c &= \frac{1}{2M}\left|\frac{\partial C_X^\star}{\partial x}\right|(V_{1x}^2 - V_{2x}^2), \\ \omega_{xx}^2 &= -\frac{1}{2M}\left|\frac{\partial^2 C_X^\star}{\partial x^2}\right| \\ &\quad\times\left[(V_{1x}^2 + V_{2x}^2) + (V_{1\phi}^2 + V_{2\phi}^2)\left(1 - \frac{4|\frac{\partial C_X}{\partial x}|^2}{C_T\frac{\partial^2 C_X^\star}{\partial x^2}}\right)\right]. \end{aligned} \tag{A9}$$

Under the orthogonality condition $\langle \chi_{1x}\chi_{2x} \rangle = 0$, the torque and its gradient are given analogously,

$$N_\phi = I\gamma_{\phi_c} - I\omega_{\phi\phi}^2\phi \tag{A10}$$

with

$$\gamma_{\phi_c} = \frac{1}{2M}\left|\frac{\partial C_X^\star}{\partial \phi}\right|(V_{1\phi}^2 - V_{2\phi}^2),$$
$$\omega_{\phi\phi}^2 = -\frac{1}{2I}\left|\frac{\partial^2 C_X^\star}{\partial \phi^2}\right| \times \left[(V_{1\phi}^2 + V_{2\phi}^2) + (V_{1x}^2 + V_{2x}^2)\left(1 - \frac{4|\frac{\partial C_X}{\partial \phi}|^2}{C_T \frac{\partial^2 C_X^\star}{\partial \phi^2}}\right)\right]. \tag{A11}$$

From these equations, we foresee an actuation scheme where the stiffness is held constant, both in x and ϕ by holding constant both $V_{1x}^2 + V_{2x}^2 = V_{\mathrm{MAX}_x}^2$ and $V_{1\phi}^2 + V_{2\phi}^2 = V_{\mathrm{MAX}_\phi}^2$. This simplifies the control dynamics, with a predictable elastic coupling that is independent of the commanded forces and torques, g_c and γ_{ϕ_c}. This also avoids conversion of a varying torque command into force noise for a translated TM; the force just depends on the TM translation offset, not on the torque command.

The commanded forces per unit mass, sensitive to the difference $(V_{1x}^2 - V_{2x}^2)$ and programmed by the force to voltage conversion in Eq. (3), are bounded by the range $\pm g_0$, with force authority g_0 given by

$$g_0 = \frac{1}{2m}\left|\frac{\partial C_X^\star}{\partial x}\right| V_{\mathrm{MAX}_x}^2. \tag{A12}$$

The maximum positive (or negative) force is obtained for $V_{1x} = V_{\mathrm{MAX}_x}$ (or $V_{2x} = V_{\mathrm{MAX}_x}$) and the other voltage V_{2x} or V_{1x} set to zero, essentially pulling only on the positive (or negative) X face of the TM. A null force is commanded by setting $V_{1x} = V_{2x} = \frac{V_{\mathrm{MAX}_x}}{\sqrt{2}}$. The angular accelerations are similarly bounded, with authority

$$\gamma_{\phi_0} = \frac{1}{2I}\left|\frac{\partial C_X^\star}{\partial \phi}\right| V_{\mathrm{MAX}_\phi}^2. \tag{A13}$$

The stiffnesses, translational and rotational, can be expressed in terms of these force and torque authorities,

$$\omega_{xx}^2 = -\frac{|\frac{\partial^2 C_X^\star}{\partial x^2}|}{|\frac{\partial C_X^\star}{\partial x}|}\left[g_0 + R_\phi^\star \gamma_{\phi_0}\left(1 - \frac{4|\frac{\partial C_X}{\partial x}|^2}{C_T \frac{\partial^2 C_X^\star}{\partial x^2}}\right)\right],$$
$$\omega_{\phi\phi}^2 = -\frac{|\frac{\partial^2 C_X^\star}{\partial \phi^2}|}{|\frac{\partial C_X^\star}{\partial \phi}|} \times \left[\gamma_{\phi_0} + \frac{g_0}{R_\phi^\star}\left(1 - 4\frac{|\frac{\partial C_X}{\partial \phi}|^2}{C_T \frac{\partial^2 C_X^\star}{\partial \phi^2}}\right)\right]. \tag{A14}$$

The prefactor setting the relationship between the x axis authority g_0 and the stiffness ω_{xx}^2 can be approximated geometrically, $\frac{|\frac{\partial^2 C_X^\star}{\partial x^2}|}{|\frac{\partial C_X^\star}{\partial x}|} \approx \frac{2}{d_x}$, roughly $6 \times 10^{-7}/\mathrm{s}^2$ per nm/s^2 of force authority. The contributions of both force and torque authority to the translational stiffness were measured in flight by LPF [17] and confirmed finite-element analyses [25] at the level of several percent.

To limit both the force gradients and the force noise arising from actuation, the strategy in both LPF and LISA is that of reducing the authorities g_0 and γ_{ϕ_0} to the minimum levels allowing compensation of the intrinsic DC forces—in both cases mainly the residual error from spacecraft gravitational balancing [4]—with some margin for any controller dynamics.

2. Remaining actuation noise and imperfections

Deviations of the applied actuation voltages from the desired values create force noise in LISA Pathfinder and LISA. We model the true applied voltage $V_j(t)$ in terms of the commanded waveform $V_{jc}(t)$,

$$V_j = V_{jc}(1 + \alpha_j(t)) + v_j(t), \tag{A15}$$

where α_j represents a gain fluctuation in the electrode j actuation circuit and noise $v_j(t)$ is the actuator additive voltage noise, independent of the applied amplitude.

From Eqs. (A4) and (A15), we can identify the force noise terms which are the subject of this article:

(i) A nonzero average (DC) value of α will result in miscalibration of the actuation force. Referring to Eq. (1) and considering a *common mode* miscalibration α^{DC} of all $4X$ electrodes, we will have

$$\lambda = 1 + 2\alpha^{DC}.$$

This static gain deviation was observed in LPF, with a measured difference of nearly 4% in the nominal voltage commands ($\lambda \approx 1.08$ [17]), though this difference is understood and expected, given the actuation circuit detailed design.

(ii) A *differential* gain offset between different electrodes can create actuation crosstalk. For instance a difference $\Delta\alpha$ in the gains between electrodes $1/4$ relative to electrodes $2/3$ would result in a spurious acceleration of roughly $R_\phi^\star \gamma_{\phi_c} \times \Delta\alpha$, cross-coupling applied ϕ torque into an x force. In LPF such a crosstalk was observed, differentially between the two TM, at a level implying $\Delta\alpha \approx 0.5\%$ [18], though this apparent actuation crosstalk was degenerate with other interferometric readout geometric cross-couplings between the apparent differential acceleration δg and the SC rotational jitter. Additional actuation crosstalk terms can arise in geometric imperfections and TM rotations.

(iii) fluctuations in the various α will create a low-frequency force error, per electrode, of

$$\delta F \approx \alpha_j \frac{\partial C_j^\star}{\partial x}\langle V_{jc}^2 \rangle.$$

This is the actuator gain noise described in Sec. III A and subject of the measurement campaign reported in Sec. III C.

(iv) Additive noise v_j at the actuation carrier frequency will mix with the carrier waveform $V_{jc}(t)$ to down-convert into force in the LISA/LPF measurement band, part of the first term in Eq. (A4) and described in Sec. III A

(v) Additive noise v_j in the LISA / LPF band will mix with DC voltages—V_{TM0}, the second term in Eq. (A4) and various stray surface potentials δV_m, fourth term in Eq. (A4)—to give in-band force noise. The first contribution, coupling to TM potential and thus charge, is addressed in the measurement campaigns presented in Sec. IV.

The role of applied actuation voltages, and their noise, in their contribution to the coupling to TM charge merits a comment here. Following the notation of Refs. [21,23], we define:

$$\frac{\partial F_x}{\partial q} \equiv -\frac{1}{C_T}\left|\frac{\partial C_X}{\partial x}\right|\Delta_x. \tag{A16}$$

Δ_x essentially represents the average electrostatic field acting on the TM, normalized to an electrostatic potential applied to a single electrode housing X electrode. Considering Eq. (A1) and both contributions from applied electrode voltages [covered by Eq. (A4)], and from stray DC surface potentials [not covered by (A4)], we find

$$\Delta_x \approx \left[\frac{1}{|\frac{\partial C_X}{\partial x}|}\sum_{m(S),n(TM)}\frac{\partial C_{mn}}{\partial x}(\delta V_m - \delta V_n)\right] + [V_1^{DC} + V_2^{DC} - V_3^{DC} - V_4^{DC}], \tag{A17}$$

for a centered TM, where V_j^{DC} is the DC actuation voltages on X electrode j.

We can thus see that the X electrode applied DC voltages can be used to balance any "intrinsic" bias Δ_x, in the top line of Eq. (A17), to null the effective coupling to the TM charge noise, as used in LPF [23]. Likewise, any in-band noise in the same electrodes will create noise in the relevant average electrostatic field,

$$\delta\Delta_x^{\mathrm{ACT}} = v_1 + v_2 - v_3 - v_4, \tag{A18}$$

which is the object of the LPF charged TM experiment presented in Sec. IV.

APPENDIX B: NOISE MODELS AND DATA ANALYSIS

1. Model of force noise from actuation gain fluctuations and data analysis technique

This appendix contains a detailed description of the actuation noise model and the MCMC fitting procedure.

As anticipated in Eqs. (11) and (15), we model the actuation contribution to the acceleration fluctuations in Δg and $\Delta\gamma_\phi$ in terms of correlated/uncorrelated gain fluctuations $\alpha, \alpha_i, \alpha_{ij}$ through coefficients a, a_i, a_{ij} for Δg and with b, b_i, b_{ij} for rotational acceleration $\Delta\gamma_\phi$. The values of these coefficients are as follows:

$$\begin{aligned}
a &= 2\Delta g,\\
a_1 &= 2g_{\mathrm{c1}},\\
a_2 &= -2g_{\mathrm{c2}},\\
a_{i1} &= \frac{(-1)^{i+1}}{2}(\bar{g}_{\mathrm{ic}} + g_{i0} + R^*\bar{\gamma}_{\phi_i c} + R^*\gamma_{\phi_{i0}}),\\
a_{i2} &= \frac{(-1)^{i+1}}{2}(\bar{g}_{\mathrm{ic}} + g_{i0} + R^*\bar{\gamma}_{\phi_i c} - R^*\gamma_{\phi_{i0}}),\\
a_{i3} &= \frac{(-1)^{i+1}}{2}(-\bar{g}_{\mathrm{ic}} - g_{i0} + R^*\bar{\gamma}_{\phi_i c} - R^*\gamma_{\phi_{i0}}),\\
a_{i4} &= \frac{(-1)^{i+1}}{2}(-\bar{g}_{\mathrm{ic}} - g_{i0} + R^*\bar{\gamma}_{\phi_i c} + R^*\gamma_{\phi_{i0}}),\\
b &= 2\Delta\gamma_\phi,\\
b_1 &= 2\gamma_{\phi_{\mathrm{c1}}},\\
b_2 &= -2\gamma_{\phi_{\mathrm{c2}}},\\
b_{i1} &= \frac{a_{i1}}{R^*}, \qquad b_{i4} = \frac{a_{i4}}{R^*},\\
b_{i2} &= -\frac{a_{i2}}{R^*}, \qquad b_{i3} = -\frac{a_{i3}}{R^*}.
\end{aligned} \tag{B1}$$

In our chosen actuation gain noise parametrization, discussed in Sec. III A, S_α, S_{α_i}, $S_{\alpha_{ij}}$ are considered as mutually uncorrelated. The PSD of Δg and $\Delta\gamma_\phi$ at frequency f can thus be expressed as

$$\begin{aligned}
S_{\Delta g}^{\mathrm{ACT}}(f) &= AS_\alpha(f) + \sum_{i=1,2}A_iS_{\alpha_i}(f) + \sum_{ij}A_{ij}S_{\alpha_{ij}}(f),\\
S_{\Delta\gamma_\phi}^{\mathrm{ACT}}(f) &= BS_\alpha(f) + \sum_{i=1,2}B_iS_{\alpha_i}(f) + \sum_{ij}B_{ij}S_{\alpha_{ij}}(f),\\
S_{\Delta g,\Delta\gamma_\phi}^{\mathrm{ACT}}(f) &= CS_\alpha(f) + \sum_{i=1,2}C_iS_{\alpha_i}(f) + \sum_{ij}C_{ij}S_{\alpha_{ij}}(f),
\end{aligned} \tag{B2}$$

with

$$\begin{aligned}
A &= a^2, \qquad A_i = a_i^2, \qquad A_{ij} = a_{ij}^2,\\
B &= b^2, \qquad B_i = b_i^2, \qquad B_{ij} = b_{ij}^2,\\
C &= ab, \qquad C_i = a_ib_i, \qquad C_{ij} = a_{ij}b_{ij}.
\end{aligned} \tag{B3}$$

Equation (B2) holds in any configuration of forces and authorities for LPF, including the four experiments with enhanced actuation; each experiment has *its own* A, B, C

coefficients, calculated from the averaged force/torque commands and authorities. We introduce the index q to label the four different experiments (UURLA, nominal, big, big + offset). Furthermore, it is useful to rewrite all the previous quantities in matrix formulation, for which we introduce,

$$\mathbf{S}^{\mathrm{ACT}}(f,q)=\begin{bmatrix} S^{\mathrm{ACT}}_{\Delta g}(f,q) & S^{\mathrm{ACT}}_{\Delta g,\Delta\gamma_\phi}(f,q) \\ S^{\mathrm{ACT}}_{\Delta g,\Delta\gamma_\phi}(f,q) & S^{\mathrm{ACT}}_{\Delta\gamma_\phi}(f,q) \end{bmatrix}. \tag{B4}$$

Note that the off-diagonal terms (cross-correlations) are assumed to be real; in the hypothesis that net torques and forces arise from the same forces acting locally, then any force-torque correlation would be free of delays and thus result in a real value of the cross-spectrum.

We then also introduce the coefficients matrix,

$$\mathbf{a}(q)=\begin{bmatrix} a & b \\ a_1 & b_1 \\ a_2 & b_2 \\ a_{11} & b_{11} \\ \cdots & \cdots \\ a_{24} & b_{24} \end{bmatrix}, \tag{B5}$$

and the noise generators matrix

$$\mathbf{S}_\alpha(f)=\begin{bmatrix} S_\alpha & & & & & \\ & S_{\alpha_1} & & & 0 & \\ & & S_{\alpha_2} & & & \\ & & & S_{\alpha_{11}} & & \\ & 0 & & & \cdots & \\ & & & & & S_{\alpha_{24}} \end{bmatrix}, \tag{B6}$$

actuation noise model (B2) is then rewritten as

$$\mathbf{S}^{\mathrm{ACT}}(f,q)=\mathbf{a}^T(q)\mathbf{S}_\alpha(f)\mathbf{a}(q). \tag{B7}$$

$\mathbf{a}(q)$ is a 11×2 matrix, containing all the known coefficients in (B1), that depend only on the actuation forces (index q), while $\mathbf{S}_\alpha(f)$ is a diagonal 11×11 matrix which contains the actuator gain noise PSDs at frequency f, which we will then want to extract by fitting the experimental data.

We fit our experiments to the actuation noise model in Eq. (B7), adding a possible background for force and torque noise, that is independent of the changes in actuation forces. This background actually absorbs the first actuation term—with coefficients A, B, and C—because the coupling to the relevant fully correlated gain noise S_α is essentially unchanged across these four tests. The background acceleration noise term is described as

$$\mathbf{S}^{\mathrm{bg}}(f)=\begin{bmatrix} S^{\mathrm{bg}}_{\Delta g}(f) & \xi(f)\sqrt{S^{\mathrm{bg}}_{\Delta g}(f)S^{\mathrm{bg}}_{\Delta\gamma_\phi}(f)} \\ \xi(f)\sqrt{S^{\mathrm{bg}}_{\Delta g}(f)S^{\mathrm{bg}}_{\Delta\gamma_\phi}(f)} & S^{\mathrm{bg}}_{\Delta\gamma_\phi}(f) \end{bmatrix}.$$

This allows for backgrounds in Δg and $\Delta\gamma$ that can have nonzero cross-coherence, which is modeled by parameter $\xi\in[-1,1]$. The full modeled noise is summarized as

$$\mathbf{M}(f,q)=\mathbf{S}^{\mathrm{ACT}}(f,q)+\mathbf{S}^{\mathrm{bg}}(f). \tag{B8}$$

The experimental data are ~2 day long noise time series, sampled every $T=0.1$ s, and indicated with $\Delta g[n,q]=\Delta g(t=nT,q)$ and $\Delta\gamma_\phi[n,q]=\Delta\gamma_\phi(t=nT,q)$, one couple for each of the four experiments. We divide these in $N_s(q)$, 50% overlapping stretches (110×10^3 s, labeled with s) of length N and multiply by a Blackman-Harris window $w[n]$. Then, we calculate the *modified periodograms* as in Ref. [31], for example for Δg we have

$$\begin{aligned} X_{\Delta g}[k,q,s]&=\sqrt{\frac{T}{N}}\sum_{n=0}^{N-1}\Delta g[n,q,s]w[n]e^{-i2\pi kn/N} \\ &\equiv X_{\Delta g}(f=k/NT,q,s). \end{aligned} \tag{B9}$$

The two periodograms are then grouped in the following complex column vector,

$$\mathbf{X}_s=\sqrt{2}\begin{bmatrix} X_{\Delta g}(f,q,s) \\ X_{\Delta\gamma_\phi}(f,q,s) \end{bmatrix}, \tag{B10}$$

and the experimental estimate $\hat{S}$ of the *single-sided cross spectral density* (CPSD) matrix can be expressed as

$$\hat{\mathbf{S}}(f,q)=\begin{bmatrix} \hat{S}_{\Delta g}(f,q) & \hat{S}_{\Delta g,\Delta\gamma_\phi}(f,q) \\ \hat{S}^*_{\Delta g,\Delta\gamma_\phi}(f,q) & \hat{S}_{\Delta\gamma_\phi}(f,q) \end{bmatrix}=\langle\mathbf{X}_s\mathbf{X}_s^\dagger\rangle, \tag{B11}$$

where $\langle\rangle$ indicates an average over all periodograms. The way the stretches are chosen and weighted at each frequency allows to obtain different estimates of the spectra. In this study, we do it in two ways:

(i) Standard Welch method: As in the standard Welch method [47], the spectrum is calculated at each frequency with the same number of stretches $N_s=N_s(q)$, 3 for UURLA, 2 in other tests. The frequencies that can be considered uncorrelated

using a Blackman-Harris window are $nf_{\min}$, with $f_{\min} = 4/\Delta T$ and n an integer [30]. Data from the standard Welch technique are shown as continuous lines in various spectral plots, and we use these data for the smooth frequency-dependent fits described below [around Eq. (B21)].

(ii) Minimally correlated frequencies method: This technique is used to calculate $\hat{\mathbf{S}}$ with a number of data stretches that increases with frequency, having therefore $N_s = N_s(f, q)$. This allows us to have data points with roughly equal spacing in $\log(f)$, maintaining minimal correlation. The frequencies are given by (see Supplemental Material, Ref. [18])

$$f_1 = \frac{4}{\Delta T}, \qquad f_2 = 2f_1,$$
$$f_3 = \left(\frac{5}{3}\right) f_2, \qquad f_4 = \left(\frac{5}{3}\right) f_3, \ldots. \tag{B12}$$

All of our single-frequency fits, described below, use CPSD data calculated with this method.

Our experimental data [Eq. (B11)] are described by the model in Eq. (B8), at a given frequency f by 13 parameters; actuation noises PSD S_{α_i} and $S_{\alpha_{ij}}$, plus acceleration noise backgrounds $S^{\rm bg}_{\Delta\gamma_\phi}$ and $S^{\rm bg}_{\Delta g}$ with the background correlation coefficient and ξ. As mentioned above fully correlated noise, S_α, is considered as a contribution to the unchanging background acceleration noise.

We estimate these parameters with a Bayesian approach. We indicate with $\hat{\mathbf{D}}$ the collection of all data on which we want to perform the parameter estimation with, for example, all the CPSD estimates at a single frequency $\hat{\mathbf{D}}(f) = \{\hat{\mathbf{S}}(f, q)\}_q$. The posterior distribution of our model conditioned by the observed data can then be derived using Bayes theorem,

$$p(\mathbf{M}|\hat{\mathbf{D}}) = \frac{L(\hat{\mathbf{D}}|\mathbf{M})P(\mathbf{M})}{P(\hat{\mathbf{D}})}. \tag{B13}$$

The likelihood $L(\hat{\mathbf{D}}|\mathbf{M})$ is obtained following Refs. [31,48]. Considering a single realization of $\mathbf{X}_s$ as defined in (B10), this follows a a 2-variate complex Gaussian probability distribution,

$$p_{f,q}(\mathbf{X}_s|\mathbf{M}) = \frac{1}{\pi^2|\mathbf{M}|}\exp\{-\mathbf{X}_s^\dagger \mathbf{M}^{-1}\mathbf{X}_s\}. \tag{B14}$$

Then, in Ref. [48] it is shown that the CPSD matrix defined in (B11) is distributed according to a *complex Wishart distribution*,

$$p_{f,q}(\hat{\mathbf{S}}|\mathbf{M}) = \frac{N_s^{N_s}|\hat{\mathbf{S}}|^{N_s-2}}{\tilde{\Gamma}_2(N_s)|\mathbf{M}|^{N_s}}\mathrm{etr}[-N_s\mathbf{M}^{-1}\hat{\mathbf{S}}], \tag{B15}$$

where $\mathrm{etr}[\cdot] = \exp(\mathrm{tr}[\cdot])$ and $\tilde{\Gamma}$ is the multivariate complex gamma function. Summarizing, Eq. (B15) gives the probability of observing a certain value for matrix $\hat{\mathbf{S}}$ given a theoretical CPSD $\mathbf{M}$, at a single frequency, using N_s periodograms of Δg and $\Delta\gamma_\phi$. Finally, the total probability of observing $\hat{\mathbf{D}}(f) = \{\hat{\mathbf{S}}(f, q)\}_q$ at a single frequency is

$$L_f(\hat{\mathbf{D}}|\mathbf{M}) = \prod_q p_{f,q}(\hat{\mathbf{S}}|\mathbf{M}). \tag{B16}$$

Starting from this likelihood, we perform two types of Markov chain Monte Carlo sampling (MCMC) to estimate the posterior distributions of our model parameters using Eq. (B13); first at discrete frequencies—without assuming any specific model of frequency dependence of noise—and second with a phenomenological analytic model of frequency dependence. In the first fit we consider data at a single frequency f of the minimally correlated frequencies introduced above. The ten elements in $\mathbf{S}_\alpha(f)$, plus background parameters $S^{\rm bg}_{\Delta\gamma_\phi}(f)$, $S^{\rm bg}_{\Delta g}(f)$ and $\xi(f)$ are taken as the parameters in model Eq. (B8) and samples from their joint posterior distribution are drawn using a standard Metropolis-Hastings MCMC algorithm with adaptive covariance. Priors used for these parameters are discussed in the following. To be fully agnostic in the *a priori* assumptions used in the fit, an ideal noninformative prior [32] for each of the twelve noise PSD could consist in a uniform (flat) prior on their logarithm—e.g. $\log S_{\alpha_{11}}$—essentially allowing *any* order of magnitude of the noise spectra. However, various parameters in our fit are essentially unresolved in our data. This is due to a combination of a relatively large ratio of parameters (total: 13) to the number of experimental data (12, for 3 channels between Δg, $\Delta\gamma_\phi$ and their cross-correlation, in four different measurements), to some near degeneracies in the coefficients $\mathbf{A}(\mathrm{q})$ and to the small values of some of the spectra. As such, the MCMC fit admits solutions in which some parameters are compatible with zero, or with logarithmic values that can diverge to $-\infty$; when the parameter becomes *small*, the likelihood in Eq. (B16) becomes insensitive to just *how small* and the Markov chain convergence becomes an issue.

Different approaches exist for solving this problem, including reducing the number of model parameters and inserting lower limits (cutoffs) in the *a priori* assumptions on the parameters. We have chosen a physically motivated approach that reparametrizes the actuation noise in terms of just two *average* noise PSD, for board correlated gain noise ($S_{\alpha_{\rm C}}$) and uncorrelated single electrode gain noise ($S_{\alpha_{\rm UC}}$), and a series of parameters μ_m that describe the *difference* in the noise between different noise generators,

$$
\begin{aligned}
S_{\alpha_1} &= S_{\alpha_C}(1+\mu_c),\\
S_{\alpha_2} &= S_{\alpha_C}(1-\mu_c),\\
S_{\alpha_{11}} &= S_{\alpha_{UC}}(1+\mu_\pm)(1+\mu_{tb+})(1+\mu_1),\\
S_{\alpha_{12}} &= S_{\alpha_{UC}}(1+\mu_\pm)(1-\mu_{tb+})(1+\mu_2),\\
S_{\alpha_{13}} &= S_{\alpha_{UC}}(1-\mu_\pm)(1-\mu_{tb-})(1+\mu_3),\\
S_{\alpha_{14}} &= S_{\alpha_{UC}}(1-\mu_\pm)(1+\mu_{tb-})(1+\mu_4),\\
S_{\alpha_{21}} &= S_{\alpha_{UC}}(1+\mu_\pm)(1+\mu_{tb+})(1-\mu_1),\\
S_{\alpha_{22}} &= S_{\alpha_{UC}}(1+\mu_\pm)(1-\mu_{tb+})(1-\mu_2),\\
S_{\alpha_{23}} &= S_{\alpha_{UC}}(1-\mu_\pm)(1-\mu_{tb-})(1-\mu_3),\\
S_{\alpha_{24}} &= S_{\alpha_{UC}}(1-\mu_\pm)(1+\mu_{tb-})(1-\mu_4),
\end{aligned}
\tag{B17}
$$

where all parameters μ_m are constrained to the interval $\mu_m \in [-1,1]$. For instance, $\mu_\pm = 0$ would imply that the $+X$ and $-X$ actuators are equally noisy, while $\mu_\pm = \pm 1$ implies that the total sum of the uncorrelated gain noise comes from the $+X$ (or $-X$) actuators, with the other group completely noiseless. We keep the uninformative log-flat prior in the PSDs S_{α_C} and $S_{\alpha_{UC}}$, with however a uniform (flat) prior for the μ_m across the interval $[-1,1]$. This allows exploring orders of magnitude in the average noise, but makes it improbable that, for instance, a single electrode actuator might be many orders of magnitude noisier than another electrode (or that the board-correlated gain noise for TM1 be many orders of magnitude quieter than that for TM2). As the electrode actuation circuits are nominally identical, we consider this a physically reasonable hypothesis.

In this parametrization we write the combined actuator quantities that are presented in Figs. 6 and 7, considering their definitions in Eqs. (16) and (19):

$$
\begin{aligned}
S_{\alpha_{UC+}} &= S_{\alpha_{UC}}(1+\mu_\pm),\\
S_{\alpha_{UC-}} &= S_{\alpha_{UC}}(1-\mu_\pm),\\
S_{\alpha_{UC14}} &= S_{\alpha_{UC}}[(1+\mu_\pm)(1+\mu_{tb+}) + (1-\mu_\pm)(1+\mu_{tb-})],\\
S_{\alpha_{UC23}} &= S_{\alpha_{UC}}[(1+\mu_\pm)(1-\mu_{tb+}) + (1-\mu_\pm)(1-\mu_{tb-})].
\end{aligned}
\tag{B18}
$$

Figure 13 shows an example of distributions of S_{α_C} and $S_{\alpha_{UC}}$, raw parameters in the parametrization of Eq. (B17) obtained from the MCMC at two relevant frequencies.

Even though the group of experiments is sensitive to S_{α_C}, the data are compatible with the hypothesis that S_{α_C} is zero (and that the overall acceleration noise is explained by uncorrelated fluctuations). Also $S^{bg}_{\Delta\gamma_\phi}$ seems to be compatible with zero at the two lowest frequencies. As a result, for these parameters a lower cutoff was still needed to ensure convergence; this was introduced using a smooth, improper prior of the form,

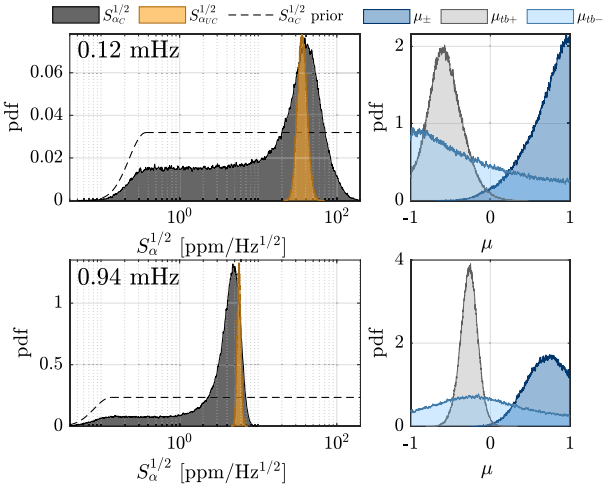

FIG. 13. Examples of distributions of $S_{\alpha_{UC}}$ (orange) and S_{α_C} (black) obtained from the MCMC fit. At both frequencies the uncorrelated electrode gain noise $S_{\alpha_{UC}}$ is robustly resolved from the experimental data and largely independent to any prior assumptions on the distribution, while the lower tail of the posterior for board-correlated gain noise S_{α_C} is only limited, in the lower values, by the prior. To allow better visualization, the former is normalized to 1, the latter to 4. The dashed line instead gives an idea of the S_{α_C} cutoff; its values have no particular meaning in this plot and should only help visualizing its position and shape. At right are distributions, at the same two frequencies, for the partitioning of the levels of uncorrelated gain noise between different groups of electrodes.

$$
P(S_{\alpha_C}) \propto \begin{cases} \exp\left[-\frac{(\log S_{\alpha_C} - \log \bar{S}_{co})^2}{2\sigma_{co}^2}\right] & \text{if } S < \bar{S}_{co} \\ 1 & \text{if } S > \bar{S}_{co}, \end{cases}
\tag{B19}
$$

where we chose $\sigma_{co} \approx 1$ and $\bar{S}_{co}$ as $1/100$ of the noise (power) declared on the data sheet for the components associated with S_{α_C} [33]. A cutoff of the same form was introduced for $S^{bg}_{\Delta\gamma_\phi}$, with the corresponding $\bar{S}^{bg}_{\Delta\gamma_\phi}$ taken as $1/100$ of the observed residual gas Brownian noise level, which is very well-understood and constitutes a solid lower limit [49]. We chose to take $1/100$ of these physically motivated lower limits to be as agnostic as possible in the parameter estimation. Figure 13 again shows that the lower tail of the distribution associated with these parameters is completely determined by the prior (therefore not constrained by observations), as the likelihood [Eq. (B16)] becomes insensitive to S_{α_C} when this is too small. While lower bounds are not resolved, upper bounds are instead very well-constrained, as demonstrated by the complete independence of the distribution peak position (and width) on the cutoff choice. Figure 13 also shows how $S_{\alpha_{UC}}$ is instead very well resolved (left panel, in orange), and some examples of relevant μ parameters (right panel). $\mu_\pm$ expresses the difference between $+X$ and $-X$ actuators,

while μ_{tb+} between $+X$ actuators which contribute positively/negatively to cross-correlation; they are both well-constrained. μ_{tb-} instead (analogous of μ_{tb+} for $-X$), is almost flat, in first place due to the fact that $-X$ electrodes happened to be less noisy than $+X$; then, also because we lack a second "big+offset" experiment enhancing only negative electrodes. One last mention to the μ_1, μ_3, μ_3, μ_4 parameters, which represent the difference between two electrodes in the same position of different TMs; these are basically not resolved, mainly due to the degeneracy of their $\mathbf{A}(q)$ coefficients. In this paper, estimates of the parameters are often reported by points with error bars (the central point is the 50th percentile while bars indicate the equally tailed 68% confidence interval), that can be seen for example in Figs. 5 and 6. While we consider our priors to be both conservative and physically motivated, we give a visual indication of the data points for model parameters in the cases where the lower limit of the posterior distribution is strongly dependent on the prior assumptions and not strongly constrained by the experimental data. We can define an effective lower limit $S_{ll}(\bar{S}_{\rm co})$ as the PSD value at the -1σ level (15.9% percentile) of the distribution. In presence of important tails like S_{α_C} in Figure 13, if the prior cutoff ($\bar{S}_{\rm co}$) is lowered of a factor 10, the lower limit $S_{ll}(\bar{S}_{\rm co})$ behaves almost exactly as if the posterior distribution were uniform (in log), decreasing by ∼86% in linear scale. We adopted, as a rule of thumb, the criteria for marking with a dash-dot line, to indicate sensitivity to the lower-cutoff prior, all the parameters estimates for which

$$\frac{S_{ll}(\bar{S}_{\rm co}/10)}{S_{ll}(\bar{S}_{\rm co})} < \frac{1}{2}. \tag{B20}$$

For these parameters, the distribution upper limit is instead much less sensitive to the prior cutoff choice, varying typically by order several percent and never more than 10% for a factor 10 increase in the upper cutoff.

The regularity of the results obtained analysing each frequency independently suggest that the whole behavior can be safely described also using smooth analytical functions of the frequency f, specifically

$$\begin{aligned} S_{\alpha_i}(f) &= \frac{\epsilon_i}{f^2 + f_{\rm cut}^2} + \frac{\rho_i}{f}, \\ S_{\alpha_{ij}}(f) &= \frac{\epsilon_{ij}}{f^2 + f_{\rm cut}^2} + \frac{\rho_{ij}}{f}, \\ S^{\rm bg}_{\Delta g}(f) &= \frac{\epsilon^{\rm bg}_{\Delta g}}{f^2} + \rho^{\rm bg}_{\Delta g}, \\ S^{\rm bg}_{\Delta\gamma_\phi}(f) &= \frac{\epsilon^{\rm bg}_{\Delta\gamma_\phi}}{f} + \rho^{\rm bg}_{\Delta\gamma_\phi} f^2. \end{aligned} \tag{B21}$$

The analytic form was chosen empirically based on the measured PSD. After reparametrizing ϵ, ρ in Eq. (B21) similarly to Eq. (B17), the MCMC runs on a total of 26 parameters. While the previous fit was performed at a single frequency, here all bins are fit at once, namely $\hat{\mathbf{D}} = \{\hat{\mathbf{S}}(f,q)\}_{f,q}$ at the frequencies, roughly 50, set by the standard Welch periodogram length. The likelihood function is exactly the same as Eq. (B16), but multiplied over all frequencies, since they are all independent,

$$L(\hat{\mathbf{D}}|\mathbf{M}) = \prod_{f,q} p_{f,q}(\hat{\mathbf{S}}|\mathbf{M}). \tag{B22}$$

Also in this case, logarithmic uniform priors were put on ϵ, ρ parameters related to average uncorrelated noise, correlated noise and background, while uniform priors were used for μ's expressing difference between different noise generators, and ξ (cross-background parameter). A lower cutoff was needed just for the two parameters associated with correlated noise, and was fixed to $1/100$ of data sheet values.

To test the goodness of our fits, we employed a posterior predictive check [35]. Assuming the distribution of the model parameters ($\mathbf{M}$) obtained from the MCMC, we derive the distributions for $\hat{\mathbf{D}}$ and then evaluate the compatibility with the experimental data. To do this, for each value of $\mathbf{M}$ accepted in the Markov chain we sample values of $\mathbf{X}_s$—the Fourier components in Δg and $\Delta\gamma_\phi$ extracted randomly for a finite length experiment—from Eq. (B14) by diagonalizing M^{-1} and expressing the elements of $\mathbf{X}_s$ in terms of independent variables, which can be easily sampled,[4] then $\hat{\mathbf{S}}$ is calculated through Eq. (B11). Once we have distributions for $\hat{\mathbf{S}}$, we calculate the $\pm\sigma$ intervals for $\hat{S}_{\Delta g}$, $\hat{S}_{\Delta\gamma_\phi}$, $\hat{S}_{\Delta g,\Delta\gamma_\phi}$ at all frequencies, for each experiment. If the fit is indeed good, then we should find that ≈68% of the experimental data fall within the posterior predicted intervals. Considering the fit performed at single frequencies, we find that ≈85% of experimental data fall in the predicted intervals; this may indicate that we are slightly overfitting by using 13 parameters at each frequency, with 12 experimental data (four separate experiments with three data, with PSD estimates for Δg, $\Delta\gamma_\phi$, and their cross-spectrum). With regard to the fit to smooth functions instead, we find 68% of experimental data falling in the posterior prediction: this result is consistent even when not considering the whole dataset, for example when estimating the goodness of fit in a single experiment, or only considering noise in the translational acceleration Δg,

[4]This 2-variate complex Gaussian distribution can be equivalently sampled by extracting real and imaginary parts of $\mathbf{X}_s$ from a 4-variate (real) Gaussian distribution [48].

indicating that the model is able to properly reproduce the observations.

2. Model of force noise from in-band fluctuations and data analysis technique

The analysis of in-band voltage fluctuations is carried out analogously to the previous subsection. We report here a quick summary of the models used. We have only two experiments, with $V_{TM} \approx 0$ V and then with $V_{TM} \approx 1$ V, which we label again with index q. In general our model for acceleration/torque PSDs and cross-spectra can be written as in Eq. (23),

$$\begin{aligned} S_{\Delta g} &= S^{\mathrm{bg}}_{\Delta g} + \left(\frac{\frac{\partial C_X}{\partial x} V_{TM}}{M}\right)^2 S_{\Delta(\Delta_x)}, \\ S_{\Delta \gamma_\phi} &= S^{\mathrm{bg}}_{\Delta \gamma_\phi} + \left(\frac{\frac{\partial C_X}{\partial \phi} V_{TM}}{I}\right)^2 S_{\Delta(\Delta_\phi)}, \\ S_{\Delta g, \Delta \gamma_\phi} &= S^{\mathrm{bg}}_{\Delta g, \Delta \gamma_\phi} + \frac{\frac{\partial C_X}{\partial x}\frac{\partial C_X}{\partial \phi} V_{TM}^2}{IM} S_{\Delta(\Delta_x),\Delta(\Delta_\phi)}. \end{aligned} \tag{B23}$$

As described in the text, an estimate of $S_{\Delta(\Delta_x)}$ can be extracted by simply fitting the first line in Eq. (B23) to the observed $S_{\Delta g}$ using $S_{\Delta(\Delta_x)}$ and $S^{\mathrm{bg}}_{\Delta g}$ as parameters, and using the one dimensional version of likelihood (B16). Same holds for $S_{\Delta(\Delta_\phi)}$ and the second line of Eq. (B23). This was done at single frequencies and also fitting smooth functions; in the first case, given the very small amount of periodograms available (therefore wide PSD distributions), a lower cutoff was needed on $S_{\Delta(\Delta_x)}$ and $S_{\Delta(\Delta_\phi)}$, fixed to the *very* conservative $1/100$ thermal limit of actuation circuits. In the hypothesis of stray electrostatics noise dominated by uncorrelated fluctuations in the electrode actuation voltages, we can summarize the PSD model in Eq. (B23), similarly to Eq. (B8) as

$$\mathbf{M}(f,q) = \mathbf{v}^T(q)\mathbf{S}_{\Delta(\Delta)}(f)\mathbf{v}(q) + \mathbf{S}^{\mathrm{bg}}(f), \tag{B24}$$

where $\mathbf{S}^{\mathrm{bg}}(f)$ is the same as that in Eq. (B8), while

$$\begin{aligned} \mathbf{v}(q) &= V_{TM}(q)\begin{bmatrix} \frac{\partial C_X}{\partial x}/M & \frac{\partial C_X}{\partial \phi}/I \\ -\frac{\partial C_X}{\partial x}/M & \frac{\partial C_X}{\partial \phi}/I \end{bmatrix}, \\ \mathbf{S}_{\Delta(\Delta)}(f) &= \begin{bmatrix} S_{\Delta(\Delta_{14})}(f) & 0 \\ 0 & S_{\Delta(\Delta_{23})}(f) \end{bmatrix}. \end{aligned} \tag{B25}$$

Finally, consistently with the approach for gain noise, we again use the hypothesis of statistically identical electrodes, writing,

$$\begin{aligned} S_{\Delta(\Delta_{14})} &= S_\Delta(1+\mu_b), \\ S_{\Delta(\Delta_{23})} &= S_\Delta(1-\mu_b). \end{aligned} \tag{B26}$$

At each minimally correlated frequency, we use the same MCMC described in the previous section with likelihood [Eq. (B16)] to estimate the distributions of the parameters S_Δ, $S^{\mathrm{bg}}_{\Delta g}$, $S^{\mathrm{bg}}_{\Delta \gamma_\phi}$ with a prior uniform in the logarithm, while μ_b and ξ [expressing the correlation between backgrounds as in Eq. (B8)] with a uniform prior distribution across the interval $[-1, 1]$.

We also perform a fit describing the relevant quantities as smooth functions of frequency. While backgrounds are written as in (B21), we write the other quantities as

$$\begin{aligned} S_{\Delta(\Delta_{14})} &= \frac{\epsilon_{14}}{f^2} + \frac{\rho_{14}}{f} + \eta_{14}, \\ S_{\Delta(\Delta_{23})} &= \frac{\epsilon_{23}}{f^2} + \frac{\rho_{23}}{f} + \eta_{23}, \end{aligned} \tag{B27}$$

and MC estimate ϵ, ρ, η after a a reparametrization similar to Eq. (B26). The results indicate that only the $1/f$ component is significantly different from zero.

[1] M. Armano *et al.*, Phys. Rev. Lett. **116**, 231101 (2016).
[2] K. Danzmann *et al.*, LISA: Laser Interferometer Space Antenna, https://www.cosmos.esa.int/documents/678316/1700384/LISA_L3_20170120+-+Submitted.pdf/5b036a72-ed33-dbad-871d-f16ed282723d (2017).
[3] F. Antonucci *et al.*, Classical Quantum Gravity **28**, 094002 (2011).
[4] M. Armano *et al.*, Classical Quantum Gravity **33**, 235015 (2016).
[5] A. Schleicher *et al.*, CEAS Space J. **10**, 471 (2018).
[6] M. Armano *et al.*, Phys. Rev. D **99**, 082001 (2019).
[7] M. Armano *et al.*, Phys. Rev. D **99**, 122003 (2019).
[8] M. Armano *et al.*, Phys. Rev. D **96**, 062004 (2017).
[9] M. Armano *et al.*, Phys. Rev. Lett. **126**, 131103 (2021).
[10] M. Armano *et al.*, Phys. Rev. D **106**, 082001 (2022).
[11] R. Rummel, W. Yi, and C. Stummer, J. Geodes. **85**, 777 (2011).
[12] W. J. Bencze, R. W. Brumley, M. L. Eglington, D. N. Hipkins, T. J. Holmes, B. W. Parkinson, Y. Ohshima, and C. W. F. Everitt, Classical Quantum Gravity **32**, 224005 (2015).

[13] P. Touboul *et al.*, Phys. Rev. Lett. **129**, 121102 (2022).
[14] W. J. Weber *et al.*, Proc. SPIE Int. Soc. Opt. Eng. **4856**, 31 (2002).
[15] R. Dolesi *et al.*, Classical Quantum Gravity **20**, S99 (2003).
[16] M. Armano *et al.*, Phys. Rev. D **98**, 062001 (2018).
[17] M. Armano *et al.*, Phys. Rev. D **97**, 122002 (2018).
[18] M. Armano *et al.*, Phys. Rev. Lett. **120**, 061101 (2018).
[19] D. N. A. Shaul, H. M. Araújo, G. K. Rochester, T. J. Sumner, and P. J. Wass, Classical Quantum Gravity **22**, S297 (2005).
[20] W. J. Weber, L. Carbone, A. Cavalleri, R. Dolesi, C. D. Hoyle, M. Hueller, and S. Vitale, Adv. Space Res. **39**, 213 (2007).
[21] F. Antonucci, A. Cavalleri, R. Dolesi, M. Hueller, D. Nicolodi, H. B. Tu, S. Vitale, and W. J. Weber, Phys. Rev. Lett. **108**, 181101 (2012).
[22] T. Sumner, G. Mueller, J. W. Conklin, P. J. Wass, and D. Hollington, Classical Quantum Gravity **37**, 045010 (2020).
[23] M. Armano *et al.*, Phys. Rev. Lett. **118**, 171101 (2017).
[24] R. Giusteri, Parabolic flights in pico-g for space-based gravitational wave observatories: The free-fall experiment on LISA Pathfinder, Ph.D. thesis, University of Trento, 2017.
[25] N. Brandt and W. Fichter, J. Phys. Conf. Ser. **154**, 012008 (2009).
[26] M. Armano *et al.*, Rev. Sci. Instrum. **91**, 045003 (2020).
[27] M. Bassan *et al.*, Phys. Rev. Lett. **116**, 051104 (2016).
[28] M. Bassan *et al.*, Astropart. Phys. **97**, 19 (2018).
[29] S. Anza *et al.*, Classical Quantum Gravity **22**, S125 (2005).
[30] S. Vitale *et al.*, Phys. Rev. D **90**, 042003 (2014).
[31] L. Sala, Residual test mass acceleration in LISA Pathfinder: In-depth statistical analysis and physical sources, Ph.D. thesis, University of Trento, 2023.
[32] H. Jeffreys, Proc. R. Soc. A **186**, 1007 (1946).
[33] Based on the LT1021 voltage reference, see for instance https://www.analog.com/media/en/technical-documentation/data-sheets/1021fc.pdf.
[34] M. Armano *et al.*, Mon. Not. R. Astron. Soc. **486**, 3368 (2019).
[35] A. Gelman, A. Vehtari, D. Simpson, C. C. Margossian, B. Carpenter, Y. Yao, L. Kennedy, J. Gabry, P.-C. Bürkner, and M. Modrák, arXiv:2011.01808.
[36] M. Armano *et al.*, Phys. Rev. D **107**, 062007 (2023).
[37] C. Grimani, H. Vocca, G. Bagni, L. Marconi, R. Stanga, F. Vetrano, A. Viceré, P. Amico, L. Gammaitoni, and F. Marchesoni, Classical Quantum Gravity **22**, S327 (2005).
[38] LISA Pathfinder demonstration of continuous discharge, to be published by the LISA Pathfinder Collaboration.
[39] S. P. Kenyon *et al.*, IEEE Aerospace Conference, 10.1109/AERO50100.2021.9438339 (2021).
[40] M. Armano *et al.*, Phys. Rev. Lett. **123**, 111101 (2019).
[41] In-depth analysis of LISA Pathfinder performance results: Time evolution, noise projection, physical models and implications for LISA, to be published by the LISA Pathfinder Collaboration.
[42] M. Carlesso, A. Bassi, P. Falferi, and A. Vinante, Phys. Rev. D **94**, 124036 (2016).
[43] A. L. Miller and L. Mendes, Phys. Rev. D **107**, 063015 (2023).
[44] A. Cavalleri *et al.*, Classical Quantum Gravity **26**, 094017 (2009).
[45] G. Russano *et al.*, Classical Quantum Gravity **35**, 035017 (2018).
[46] W. J. Herrera and R. A. Diaz, Am. J. Phys. **76**, 55 (2008).
[47] P. Welch, IEEE Trans. Audio Electroacoust. **15**, 70 (1967).
[48] N. R. Goodman, Ann. Math. Stat. **34**, 152 (1963).
[49] A. Cavalleri, G. Ciani, R. Dolesi, A. Heptonstall, M. Hueller, D. Nicolodi, S. Rowan, D. Tombolato, S. Vitale, P. J. Wass, and W. J. Weber, Phys. Rev. Lett. **103**, 140601 (2009).